UNIVERSITÀ POLITECNICA DELLE MARCHE
Department of Industrial Engineering and Mathematical Sciences

Master's Degree in Green Industrial Engineering

Characterization of Aluminum Alloys for Re-Shaping Applications:
Improving the Reuse of End-of-Life Components in New Part Manufacturing

Supervisor:
Prof. Marco Rossi

Degree Thesis of:
VinayKumar Gudise

Academic Year 2025 / 2026

Abstract

The direct reshaping of aluminium alloy sheet metal components at end-of-life represents a high-value circular economy strategy, preserving material properties and avoiding the energy penalty of conventional recycling through re-melting. This thesis presents a systematic numerical characterisation of thickness distribution in an aluminium alloy sheet of initial thickness 2 mm subjected to single-step and multi-step press-forming operations representing both baseline and end-of-life (EoL) reshaping scenarios.

Eight specimen configurations were investigated using two-dimensional plane strain finite element simulations carried out in Abaqus/Explicit, incorporating a Johnson-Cook constitutive model calibrated for an AA6xxx series alloy representative of automotive end-of-life components. Four baseline configurations characterised thickness distributions for single-notch geometries at two punch depths (D1: 10 mm; D2: 6 mm) and double-notch geometries pressed from virgin blanks (DN1: 8 mm; DN2: 5 mm). Four combined configurations — D1DN1, D1DN2, D2DN1, and D2DN2 — simulated the reshaping of blanks carrying prior single-notch deformation history, representing realistic end-of-life component conditions.

Nodal coordinate data was extracted from simulation output and inter-surface thickness computed using the Euclidean distance between corresponding top and bottom surface nodes. Results show that baseline configurations exhibit moderate thinning of 18.4–20.2% at bend corners, forming a tight reference band. Combined EoL configurations showed substantially greater thinning, with D1DN1 reaching 33.6% and exhibiting corner-to-corner non-uniformity roughly twenty-two times greater than baseline. A clear dependence on prior forming depth was established: blanks with deep prior history (D1, 10 mm) showed 14.1 percentage points more thinning than shallow prior history (D2, 6 mm) for the same second-press geometry. Notably, shallow prior deformation (D2) produced thinning only 1.1 percentage points above the virgin baseline, confirming reshaping feasibility. No fracture was predicted in any configuration.

A provisional safe reshaping envelope is defined: shallow prior deformation (≤6 mm) does not meaningfully compromise subsequent formability, while deep prior deformation (≥10 mm) demands careful second-press geometry selection. Geometric overlap between successive press corner positions is identified as an independent damage amplifier, independent of absolute forming depths. These findings provide the first quantitative numerical basis for defining safe reshaping envelopes for aluminium sheet components within circular economy manufacturing frameworks.

Keywords: *aluminium alloy; end-of-life reshaping; circular economy; finite element analysis; Abaqus/Explicit; Johnson-Cook; thickness distribution; multi-step forming; plane strain.*

Table of Contents

List of Figures

List of Tables

List of Abbreviations

BC: Boundary Condition
BHF: Blank Holder Force
CAE: Computer-Aided Engineering
CPS4R / CPE4R: 4-node bilinear plane stress / plane strain quadrilateral, reduced integration (Abaqus element codes — see Section 2.4.1 for a note on the present model)
DOE: Design of Experiments
EoL: End-of-Life
FE / FEA: Finite Element / Finite Element Analysis
FLC: Forming Limit Curve
FLD: Forming Limit Diagram
GHG: Greenhouse Gas
GWP: Global Warming Potential (kg CO_2-eq/kg)
IE: Internal (Strain) Energy
J-C: Johnson-Cook (constitutive model)
KE: Kinetic Energy
LCA: Life Cycle Assessment
PEEQ: Equivalent Plastic Strain (Abaqus output)
r/t: Punch corner radius to initial sheet thickness ratio
SPIF: Single Point Incremental Forming
t_0: Initial (nominal) sheet thickness (2 mm)
UTS: Ultimate Tensile Strength
YS: Yield Strength

Introduction

Industrial Context and Motivation

The global demand for aluminium has grown continuously over the past three decades, driven by widespread adoption across the automotive, aerospace, construction, and packaging sectors as a lightweight, corrosion-resistant structural material. Primary aluminium production via the Hall-Héroult electrolytic process is among the most energy-intensive manufacturing operations, consuming approximately 13–15 kilowatt-hours of electrical energy per kilogram of metal produced, generating significant greenhouse gas emissions both directly through process chemistry and indirectly through electricity generation. At global production exceeding 65 million tonnes annually, the environmental footprint of aluminium is substantial and increasingly subject to regulatory and market pressure.

The automotive sector consumes approximately 30% of total European aluminium demand, driven by vehicle lightweighting requirements and EU fleet CO_2 emission targets. A typical modern passenger vehicle contains 150–200 kg of aluminium distributed across body panels, structural members, chassis components, and powertrain castings. When such vehicles reach end-of-life after 10–15 years of service, the aluminium is typically recovered through shredding and secondary smelting, producing secondary aluminium that requires only approximately 5% of the energy of primary production. While secondary metallurgy represents a 90–95% energy reduction relative to primary production, it dissolves the component's geometry, mechanical state, and processing history — discarding the significant embedded fabrication value.

Direct reshaping of EoL components offers a further energy advantage by avoiding the re-melting step entirely. The material is formed directly into a new geometry, retaining its work-hardened microstructural state. This approach positions reshaping at the highest tier of the circular economy materials hierarchy, above conventional recycling. The technical feasibility of direct reshaping is conditioned on a rigorous understanding of the residual formability of previously deformed sheet metal — specifically, how much additional plastic deformation the material can sustain during a second forming operation before critical thinning or fracture occurs.

The European Green Deal (2019) commits the EU to climate neutrality by 2050. The EU Circular Economy Action Plan (2020) specifically identifies aluminium as a priority material and calls for strategies that retain it at higher levels of the material value hierarchy, targeting a 30% reduction in raw material consumption by 2030. Current data indicates approximately 95% of EoL automotive aluminium is routed to secondary smelting, despite the technical and environmental case for direct reshaping in a significant fraction of cases. This gap is largely attributable to the lack of quantitative data on the conditions under which reshaping is safe — precisely the gap this thesis addresses.

From an industrial economics standpoint, reshaping also reduces dependency on primary aluminium supply chains, which are geographically concentrated and subject to significant price volatility. By enabling productive reuse of EoL blanks that would otherwise be downgraded to scrap, reshaping creates direct material cost savings and strengthens supply chain resilience. For manufacturers operating under extended producer responsibility (EPR) regulations, demonstrating component-level material recirculation — rather than bulk recycling — offers compliance and reputational advantages that secondary smelting cannot provide.

Research Objectives

Despite growing interest in EoL reshaping, systematic characterisation of thickness evolution in aluminium alloy sheets during conventional press-based multi-step forming operations remains limited. Existing studies focus on advanced processes such as Single Point Incremental Forming (SPIF) and sheet hydroforming, or on single-step operations from virgin blanks. The behaviour of previously formed sheet during a second conventional press operation across a structured range of prior deformation conditions has not been systematically investigated.

This thesis addresses this gap through a numerical study comprising eight configurations. Specific objectives are:

- (i) Characterise thickness distribution profiles for single-notch and double-notch geometries from virgin blanks, establishing reference data for measuring the effect of prior history.
- (ii) Quantify cumulative thinning when EoL blanks with documented prior deformation are subjected to a second press operation across a matrix of prior depths and second-press geometries.
- (iii) Identify which combinations of prior forming depth and second-press geometry produce critical thinning and which remain within acceptable limits, providing the basis for a provisional safe reshaping envelope.
- (iv) Provide interpretive guidance for industrial EoL reshaping process design based on the numerical results.

Scope

The study is conducted entirely through finite element simulation using Abaqus/Explicit with a 2D plane strain formulation. The plane strain assumption constrains lateral deformation to zero, representing the central cross-section of a wide sheet and providing a conservative upper-bound estimate of thinning severity. The blank has initial thickness t_0 = 2 mm and length L = 100 mm. The alloy belongs to the AA6xxx series (Al-Mg-Si), modelled using a Johnson-Cook constitutive law. Physical experimental validation is identified as a priority direction for future work but falls outside the present scope.

Thickness extraction is based on post-processing of nodal coordinate data exported from Abaqus/Explicit, using the Euclidean inter-surface distance formula. The study does not extend to springback prediction, forming force analysis, or thermal effects; these are identified as future work directions.

Thesis Structure

Chapter 1 reviews relevant literature: circular economy policy context, LCA of aluminium, sheet metal forming fundamentals, work hardening in multi-step forming, existing EoL reshaping studies, and FEA modelling approaches. Chapter 2 describes the complete methodology. Chapter 3 presents results for all eight configurations. Chapter 4 provides mechanistic discussion, literature comparison, and industrial implications. Chapter 5 presents conclusions, practical recommendations, and a future work roadmap. References follow.

Chapter 1 — State of the Art

1.1 The Circular Economy: Policy Framework and Environmental Targets

The circular economy concept represents a systemic response to resource scarcity and environmental degradation arising from the linear take-make-dispose production model. For metallic materials, the hierarchy of preferred outcomes is: direct reuse (highest value), remanufacturing to original specification, reshaping into new geometries, and finally recycling via re-melting (lowest value tier within the material loop). The concept has been operationalised into European policy through the EU Circular Economy Action Plan (CEAP, 2020) and the European Green Deal (2019), both of which identify aluminium as a priority material.

The CEAP targets a 30% reduction in raw material consumption in the EU by 2030 and identifies automotive aluminium sheet as a priority stream, estimated to represent 10–15 million tonnes of EoL components globally per year. Approximately 95% of this material is currently routed to secondary smelting, despite the environmental case for direct reshaping. Cooper and Allwood (2012) estimated that roughly 40% of EoL steel and aluminium components could be directly reused or reshaped without re-melting, based on geometric and mechanical assessment of end-of-life component inventories. Converting even a fraction of currently smelted EoL aluminium to reshaping would represent multi-million tonne annual CO_2 savings at European automotive scale.

A practical regulatory obstacle to reshaping at scale, distinct from the technical formability questions addressed in this thesis, is the "end-of-waste" classification under EU waste law. Material recovered from an end-of-life vehicle is, by default, legally classified as waste, and waste-classified material is subject to additional regulatory handling requirements (permits, tracking, restricted transport) that do not apply to virgin material or to material that has achieved "end-of-waste" status through a recognised recovery process. Secondary smelting is well-established as an end-of-waste route for aluminium under existing EU criteria, since re-melting produces a standardised ingot product indistinguishable from primary metal. Direct reshaping, by contrast, does not melt the material and therefore does not fit neatly into existing end-of-waste criteria developed with smelting in mind; clarifying the regulatory status of directly reshaped EoL components is recognised in the circular economy policy literature as a parallel barrier to the technical formability barrier this thesis addresses, though resolving it lies outside the scope of an engineering thesis and is not pursued further here.

1.2 Life Cycle Assessment of Aluminium Manufacturing Routes

Published LCA studies consistently show that primary production dominates the lifecycle environmental burden of aluminium products. Global warming potential (GWP) estimates for primary aluminium production range from 8 to 17 kg CO_2-eq/kg depending on the electricity grid mix: Northern Europe with hydroelectric power achieves 4–6 kg CO_2/kg; coal-based regions reach 17 kg CO_2/kg; the global production-weighted average is approximately 12 kg CO_2/kg. Secondary production from scrap via re-melting requires only 0.5–1.0 kg CO_2-eq/kg — a 90–95% reduction — representing one of the largest single environmental improvement opportunities in manufacturing.

Direct reshaping eliminates the re-melting step entirely. Ingarao et al. (2017) estimated that reshaping could reduce total embodied energy by 60–70% compared to the recycling-and-refabrication route, corresponding to avoided emissions of 1–3 kg CO_2-eq per kilogram of component. At the scale of the European automotive sector — approximately 3 million tonnes of EoL aluminium body panels annually — systematic adoption could avoid 3–9 million tonnes of CO_2-eq per year. Baudouin et al. (2020) confirmed a 65% GWP reduction for reshaping versus secondary smelting even accounting for transport, identifying uncertainty in residual formability as the principal barrier to industrial deployment — the barrier directly addressed by this thesis.

A methodological note on LCA system boundaries is relevant to interpreting the GWP figures cited above. The reshaping-versus-smelting comparisons in the cited studies are typically conducted on a "cradle-to-gate" or "gate-to-gate" basis — covering the recovery and reprocessing stage itself — rather than a full cradle-to-grave assessment including the use-phase performance of the resulting component. This is an appropriate boundary choice for comparing processing routes for a materially equivalent output, but it does not capture potential differences in component service life or in-service performance between a reshaped and a virgin-formed part, which would require a full comparative life cycle assessment extending beyond the scope of the present thesis. The feasibility study presented in Chapters 2 through 4 — establishing the thinning and fracture-risk envelope for reshaping — is a necessary precondition for any such full LCA to be conducted on a sound technical basis, since a part that fails prematurely in service due to excessive thinning would erode or reverse the processing-stage GWP advantage quantified by Ingarao et al. (2017) and Baudouin et al. (2020).

1.3 Aluminium Alloys: Composition, Temper, and EoL Condition

The 6xxx series (Al-Mg-Si) alloys dominate automotive sheet applications owing to their combination of medium-high strength, corrosion resistance, and precipitation hardenability. AA6016, AA6022, and AA6111 are commonly specified for outer body panels; AA6082 and AA6181 for structural inners. These alloys contain 0.3–1.5% Mg, 0.5–1.2% Si, and small secondary additions, with total alloying content typically below 2.5%.

The precipitation sequence progresses from solid solution through GP zones, β″ (Mg_5Si_6 needles, primary strengthening phase), β′, to equilibrium Mg_2Si. The T4 temper (solution treated, naturally aged) gives yield strength 120–160 MPa with elongation 22–28% — the condition for original automotive stamping. The T6 temper (peak artificially aged at 175–180°C) gives yield strength 240–280 MPa with elongation 8–12% — the condition after the paint bake cycle in vehicle assembly. For EoL components, the condition at reshaping time is the T6 service temper, further modified by service fatigue cycles. This higher yield stress and lower ductility relative to original T4 further constrains residual formability for reshaping operations — the starting condition assumed conservatively in this study.

Anisotropy from rolling texture is characterised by the Lankford r-value (ratio of width to thickness strain in tension), typically 0.6–0.8 for rolled 6xxx alloys. The Hill (1948) anisotropic yield criterion captures this through directionally dependent yield stress coefficients. For the 2D plane strain simulations of this study, the isotropic von Mises criterion is an appropriate and well-justified simplification, as lateral strain is precluded by the plane strain constraint.

1.3.1 Comparison with Other Automotive Sheet Alloy Families

While this thesis focuses on AA6xxx, two other aluminium alloy families are relevant to automotive sheet and warrant brief comparison to contextualise the alloy choice and to motivate the multi-alloy extension proposed as future work (Section 5.4, Priority 5). The 5xxx series (Al-Mg, non-heat-treatable) is typically supplied in H-temper (strain hardened) rather than T-temper, relying entirely on solid solution strengthening from magnesium content (typically 2.5–5.5% Mg) and dislocation strengthening from cold work, with no precipitation hardening response. This gives 5xxx alloys a notably higher strain hardening exponent ($n = 0.25–0.35$) than 6xxx in T6 condition, meaning 5xxx sheet continues to work-harden substantially through large strains rather than reaching a comparatively flat flow stress plateau — a property that is generally favourable for multi-step forming, since it should redistribute strain away from already-deformed regions more effectively than 6xxx, potentially producing an even more forgiving prior-history effect than the D2DN1 finding of this thesis. AA5754 and AA5182 are the most common automotive 5xxx grades, used for inner panels and structural reinforcements where the higher springback and slightly lower formability ceiling of 5xxx relative to 6xxx are acceptable trade-offs against lower cost and the absence of any paint-bake-dependent strengthening step.

The 7xxx series (Al-Zn-Mg, heat-treatable) offers the highest strength of common automotive aluminium alloys — yield strengths of 350–500 MPa in T6 or T76 temper — but at the cost of markedly reduced ductility (elongation typically 8–14%) and known susceptibility to stress corrosion cracking in some tempers, which has historically limited 7xxx adoption to high-performance structural applications (crash members, some closure reinforcements) rather than general body panel use. For EoL reshaping purposes, the combination of high initial strength and low ductility in 7xxx would be expected to produce the least forgiving reshaping envelope of the three families: less residual strain capacity is available to absorb a second-press operation, and the higher flow stress would generate proportionally higher contact forces and tooling wear in conventional press reshaping. Table 1.1 summarises the comparative mechanical character of the three alloy families as it bears on reshaping feasibility.

Table 1.1 — Comparative mechanical character of automotive aluminium sheet alloy families relevant to EoL reshaping feasibility.

Property	5xxx (Al-Mg)	6xxx (Al-Mg-Si)	7xxx (Al-Zn-Mg)
Typical temper	H32–H34	T4 (forming) / T6 (service)	T6 / T76
Yield strength range	100–200 MPa	120–280 MPa (T4–T6)	350–500 MPa
Elongation range	18–28%	8–28% (T6–T4)	8–14%
Hardening exponent n	0.25–0.35	0.08–0.26 (T6–T4)	0.05–0.15
Heat-treatable	No	Yes	Yes
Typical automotive use	Inner panels, reinforcements	Outer body panels, structural inners	High-performance structural, crash members
Expected reshaping forgiveness (qualitative)	Highest	Moderate (this study)	Lowest

This comparison is qualitative and based on general alloy mechanical character rather than dedicated EoL reshaping simulation, since — as established in Section 1.7 — no prior systematic reshaping study exists for any of these three families under conventional press conditions. The present thesis's focus on AA6xxx reflects its dominant share of automotive outer body panel production (Section 1.1) rather than an assumption that it is necessarily the most or least favourable alloy for reshaping; establishing the alloy-dependence of the reshaping envelope quantitatively is precisely the gap identified for future work.

1.4 Sheet Metal Forming: Mechanics and Thickness Evolution

1.4.1 Strain State and Volume Conservation

The mechanics of sheet thinning are governed by plastic volume conservation: $\varepsilon_1 + \varepsilon_2 + \varepsilon_3 = 0$, where ε_1 is the major in-plane strain (tensile), ε_2 the minor in-plane strain, and ε_3 the thickness strain (always negative). Under plane strain conditions ($\varepsilon_2 = 0$), all deformation partitions between major stretching and thickness reduction: $\varepsilon_1 = -\varepsilon_3$. This maximises thinning rate for a given surface strain and represents the most critical strain path for necking — the conservative bound adopted in this study.

At bend corners, deformation is a superposition of bending and membrane stretching. The outer fibre bending strain is $\varepsilon_b = t/(2r)$, where t is sheet thickness and r is tool radius. For the present geometry (t = 2 mm, punch radius ~3–5 mm), outer-fibre bending strains of 0.2–0.33 are expected, which combined with membrane stretching produce the 17–34% thinning values observed. The strain rate in the punch-sheet contact zone can reach 1–100 s^{-1} even under nominally quasi-static conditions, activating the strain rate sensitivity term in the Johnson-Cook formulation.

1.4.2 The Forming Limit Diagram and Failure Assessment

The Forming Limit Diagram (FLD), introduced by Keeler and Backofen (1963) and Goodwin (1968), maps safe and unsafe combinations of major and minor strain. The Forming Limit Curve (FLC) defines the necking boundary. For 6xxx series in T4 temper, the plane strain FLC minimum ($\varepsilon_2 = 0$) falls at major strains of 0.15–0.25; for T6 temper (the EoL service condition), it is lower at 0.10–0.18. Multi-step forming shifts the material's starting position on the FLD upward — consuming strain margin before the second operation begins — and is the primary mechanism by which EoL reshaping elevates fracture risk relative to virgin blank forming.

1.4.3 Springback

Springback — elastic strain recovery upon load removal — is proportional to σ_y/E. For AA6xxx T6 ($\sigma_y \approx 250$ MPa, E = 69 GPa), $\sigma_y/E \approx 0.0036$, approximately 2.4× higher than mild steel. In multi-step forming, residual stresses from the first operation modify the springback response of the second, producing spatially non-uniform geometry deviation not predicted by single-step analysis. Springback prediction requires an Abaqus/Implicit relaxation step not performed in this study; it is identified as a priority future work item.

1.4.4 Friction and Tribology in Sheet Forming

Friction at the punch-sheet and die-sheet interfaces governs the partition of forming load between bending and membrane stretching, and is therefore a first-order influence on thinning distribution alongside the r/t ratio discussed above. Under high friction, material at the punch nose is effectively locked against the tool surface, forcing nearly all subsequent deformation into localised bending and stretching at the corner radius rather than permitting material draw-in from adjacent flat regions; this concentrates thinning. Under low friction, the blank can slide more freely relative to both tools, distributing strain over a larger material volume and reducing peak corner thinning at the cost of increased net displacement of the blank during forming.

Published friction coefficients for aluminium sheet forming against steel tooling range from $\mu \approx 0.05–0.08$ for well-lubricated conditions (mineral oil or dedicated forming lubricant, smooth tool surface finish) to $\mu \approx 0.15–0.25$ for dry or poorly lubricated conditions, with galling risk increasing sharply above this range due to aluminium's tendency to adhere to steel tool surfaces under high contact pressure — a tribological concern specific to aluminium forming that is less severe for steel sheet against steel tooling. Surface treatments such as tool nitriding, DLC (diamond-like carbon) coating, or PVD coatings are commonly used in production aluminium stamping specifically to suppress galling and maintain a stable, low friction coefficient over a tool's service life, since friction coefficient drift over repeated press strokes is a recognised quality control concern in aluminium body panel manufacturing.

For the present study, $\mu = 0.1$ was selected as representative of a lubricated aluminium-on-steel interface, situated toward the lower end of the dry-to-lubricated range cited above (Section 2.4.2). As discussed quantitatively in Section 4.8, this parameter was not independently verified for the specific tooling and lubricant condition implied by the study, and a ±50% variation is estimated to produce a corresponding ±3–5 percentage point variation in absolute corner thinning — making friction coefficient verification, alongside mesh convergence and energy balance, one of the three standard validation steps recommended for the model reconstruction effort proposed as Priority 0 in Section 5.4.

1.5 Work Hardening and Multi-Step Forming Effects

1.5.1 Isotropic Hardening and Residual Ductility

The plastic flow stress of aluminium alloys under monotonic loading follows $\sigma = K\varepsilon^{n}$, where n = 0.20–0.26 for 6xxx T4 (lower for T6). The Johnson-Cook model extends this with a multiplicative strain rate term: $\bar{\sigma} = (A + B\bar{\varepsilon}^{n})(1 + C\ln(\dot{\bar{\varepsilon}}/\dot{\varepsilon}_0))$. In multi-step forming, the first operation raises flow stress in deformed regions (work hardening) and consumes a fraction of total plastic strain capacity (residual ductility reduction). When the second operation engages pre-hardened regions, plastic flow initiates at a higher stress and proceeds more rapidly to critical thinning. The D1 prior press (10 mm) deposits approximately 18–20% PEEQ at corners; D2 (6 mm) deposits 10–12%. This difference in consumed ductility is the mechanistic basis for the divergent outcomes between D1-based and D2-based combined configurations.

1.5.2 The Bauschinger Effect

The Bauschinger effect — yield stress reduction upon load reversal after prior plastic deformation — is pronounced in aluminium alloys, with reverse-direction yield reductions of 20–40% after 10% pre-strain. In multi-step press forming, bending-induced compression in the first operation may be followed by tension in the second (or vice versa), activating partial stress reversal. The Johnson-Cook isotropic hardening model does not capture this effect, overestimating flow stress during reverse loading and slightly underestimating PEEQ accumulation in stress-reversal regions. The estimated error magnitude is 5–10% in PEEQ — insufficient to change qualitative conclusions but noted as a limitation.

1.6 Finite Element Modelling of Sheet Forming

1.6.1 2D Plane Strain vs. 3D Shell Formulations

Two-dimensional plane strain elements model forming as a problem in a single cross-sectional plane with no out-of-plane strain, appropriate for straight-geometry tooling at the central cross-section of a wide blank. (A specific note on the element type code recovered for the present model, and an internal inconsistency between that code and the plane strain assumption, is given in Section 2.4.1.) The primary advantage of the 2D idealisation, whichever planar formulation is ultimately confirmed, is computational efficiency — a 2D model solves in minutes, enabling parametric studies across eight configurations. Three-dimensional shell element models (S4R) capture finite blank width and lateral material flow, producing 5–15% lower corner thinning than 2D predictions. The 2D results are therefore expected to be conservative upper bounds relative to a finite-width 3D blank — a desired property for an initial feasibility assessment.

1.6.2 Explicit Time Integration and Mass Scaling

Abaqus/Explicit uses the central difference explicit time integration scheme, computing accelerations element-by-element without global matrix inversion — efficient for large models with complex contact. The stable time increment is bounded by $\Delta t \leq L_{min}/c_d$, where L_{min} is the smallest element dimension and c_d is the dilatational wave speed (for aluminium, $c_d \approx 5100$ m/s). Mass scaling — artificial density increase — permits larger time steps by reducing c_d, making forming simulations tractable. The standard validity criterion is KE < 5–10% of IE throughout the simulation; as discussed in Section 2.4.4, this check could not be performed retrospectively for the present study following the loss of the original model files, and is flagged as an open verification item.

1.6.3 Contact Convergence and Common Numerical Pitfalls

Beyond mass scaling and time increment stability, surface-to-surface contact algorithms in Abaqus/Explicit are subject to several well-documented numerical pitfalls that are relevant context for interpreting the present results and for the model reconstruction effort proposed in Section 5.4. Excessive penetration between contacting surfaces — exceeding roughly 1–2% of the smallest element dimension — typically indicates either an undersized contact stiffness (for penalty-based formulations) or excessive mass scaling distorting the kinematic contact enforcement used in this study (Section 2.4.2), and is a standard diagnostic checked alongside the energy balance during model verification.

A second common pitfall specific to bending-dominated forming simulations, including the present study's notch-pressing geometry, is element distortion at the punch corner radius as the local curvature increases through the forming step. Severe distortion (element aspect ratio beyond approximately 10:1, or internal angles departing substantially from 90°) degrades the accuracy of stress and strain interpolation within the element and can, in extreme cases, trigger negative element volume errors that terminate the analysis. This is precisely the mechanism responsible for the nodal-distance extraction artefacts discussed in Section 2.5, where post-processing thickness values exceeding the nominal 2.0 mm were identified and excluded; their presence is itself indirect evidence of locally severe element distortion at the affected corners, consistent with the high curvature expected at bend radii of the magnitude investigated in this study.

A third consideration, particularly relevant to the combined (two-step) configurations of this thesis, is the numerical treatment of the transition between the first and second forming steps. Where the deformed mesh and stress/strain state from Step-1 are carried forward as the initial condition for Step-2 — the approach implied by the combined-configuration methodology described in Section 3.2 — any residual contact penetration, element distortion, or unconverged dynamic oscillation present at the end of Step-1 is inherited by Step-2 and can compound through the second forming operation. This is a further reason why the combined configurations, and particularly the most severely deformed D1DN1 and D2DN2 cases, would benefit most from the mesh convergence and energy balance re-verification proposed as the immediate next step for this work (Section 5.4, Priority 0): the baseline (single-step) configurations are comparatively low-risk for this class of numerical artefact, since they do not carry forward state from a prior, already-distorted deformation increment.

1.7 Prior Work on End-of-Life Reshaping

1.7.1 Single Point Incremental Forming Studies

SPIF has been the most extensively studied process for EoL reshaping owing to its flexibility and suitability for low-volume, variable-geometry operations. Pellegrini, Volk, and Fratini (2020) conducted a landmark study on SPIF-based EoL reshaping of deep-drawn AA2024-O aluminium components, finding that thickness in the reshaped component correlates directly with prior equivalent plastic strain distribution. Multiply-formed regions exhibited thinning 2–3 times greater than single-step baseline values. This finding — that prior PEEQ is the primary determinant of reshaping outcome — is the central mechanistic hypothesis tested and confirmed in the present conventional press study.

1.7.2 Sheet Hydroforming Studies

Piccininni et al. (2024) examined reshaping of pre-formed AA5754-O blanks via sheet hydroforming, showing that non-uniform thickness and work-hardened zones from prior forming create heterogeneous forming conditions. The pressure-displacement response differed significantly from virgin blank hydroforming, requiring process parameter adjustment. Their findings qualitatively support the present study's observation that prior forming history alters the second-operation response, though the sensitivity appears higher for hydroforming than for rigid-tool conventional pressing.

1.7.3 Conventional Press Reshaping: The Literature Gap

Despite conventional press forming accounting for over 95% of automotive body panel production, systematic investigation of EoL reshaping via conventional press tooling is absent from the literature. Published forming studies address single-step operations on virgin blanks, and the EoL reshaping studies that do exist focus on SPIF and hydroforming. The mechanical conditions in conventional press reshaping of pre-formed EoL blanks — complex initial contact geometry, pre-existing residual stress, heterogeneous thickness — differ fundamentally from standard stamping and constitute a genuinely novel problem requiring dedicated investigation. This thesis addresses this gap directly.

1.8 Damage Mechanics and Fracture Criteria for Sheet Forming

1.8.1 Ductile Damage Initiation Models

Beyond the empirical Forming Limit Diagram approach described in Section 1.4.2, mechanistic ductile damage models provide an alternative, physically motivated framework for predicting fracture initiation in sheet forming. The Gurson-Tvergaard-Needleman (GTN) model treats the material as a porous continuum in which microvoids nucleate, grow, and coalesce under plastic straining, with the void volume fraction f tracked as an internal state variable that progressively degrades the load-bearing cross-section until catastrophic failure occurs at a critical value f_c. For aluminium alloys, published f_c values range from 0.01 to 0.05 depending on alloy purity and second-phase particle content, with cleaner alloys (lower iron and silicon impurity levels) tolerating higher void fractions before coalescence.

The Johnson-Cook framework itself includes an optional companion damage model — distinct from the flow stress model used in this study — in which a damage parameter D accumulates as a function of stress triaxiality, strain rate, and temperature, with element deletion triggered at D = 1. This damage formulation was not activated in the present simulations; the Johnson-Cook model was used purely as a flow stress (hardening) law, with feasibility assessed qualitatively against published failure strain data rather than through an activated damage-and-deletion criterion. Activating the full Johnson-Cook damage model, calibrated against AA6xxx fracture data, is identified as a natural extension for future quantitative fracture risk assessment (Section 5.4).

1.8.2 Stress Triaxiality and Its Role in Multi-Step Forming

Stress triaxiality — the ratio of mean (hydrostatic) stress to von Mises equivalent stress — is a first-order control variable in ductile fracture, with most ductile damage models predicting reduced failure strain at higher triaxiality. Sheet bending operations of the type studied here typically generate low-to-moderate triaxiality (approximately 0 to 0.4) at the outer bend fibre, where the dominant stress state is uniaxial-to-biaxial tension, placing bend-corner fracture risk well below that of notched-bar or punch-shear tests, which can reach triaxiality values above 0.6. This relatively benign triaxiality regime is one reason why the substantial thinning observed in the combined configurations of this study (up to 33.6% in D1DN1) does not in itself imply imminent fracture: the strain path, not merely the strain magnitude, determines proximity to failure.

In multi-step forming, the stress state at a given material point may change character between operations — for example, transitioning from primarily bending-dominated triaxiality in the first press to membrane-stretch-dominated triaxiality in the second. This path-dependence is not captured by simple thinning-percentage thresholds and is a further argument, beyond the FLC limitations discussed in Section 1.4.2, for treating the present thinning results as indicative rather than as a definitive fracture safety certification.

1.9 Digital Manufacturing and Traceability for EoL Reshaping

A practical precondition for industrial deployment of the prior-history-dependent reshaping framework developed in this thesis is the availability of forming history data at the individual component level. Modern automotive stamping lines increasingly incorporate in-line sensing — force-displacement monitoring, optical strain mapping (digital image correlation), and thickness gauging — that generates exactly the kind of PEEQ and geometry data needed to classify EoL components by prior deformation severity, as proposed in Section 4.9. However, this data is generated and stored at the original-manufacturing stage and is rarely retained or transmitted through the vehicle service life to the point of EoL disassembly, decades later and often by an entirely different organisation.

Material passports and digital product passport (DPP) frameworks, mandated under the EU Ecodesign for Sustainable Products Regulation (ESPR, 2024) for an expanding range of product categories, offer a policy-level mechanism to close this data gap. A digital product passport for an automotive aluminium panel could in principle carry forward the original forming process parameters — punch depth, notch geometry, even simulated or measured PEEQ distribution — from the OEM's manufacturing execution system through the vehicle's service life to an EoL recovery facility, enabling exactly the depth-based sorting and corner-overlap avoidance interventions recommended in Section 4.9 without requiring new physical measurement at the point of reshaping. In the absence of such passport data — the realistic condition for the large majority of vehicles currently reaching end-of-life, which were manufactured before DPP requirements existed — the sorting classification proposed in this thesis would instead need to rely on physical measurement (e.g., portable thickness gauging or 3D scanning of the EoL component) performed at the recovery facility itself, adding cost and processing time relative to a passport-enabled workflow.

This thesis does not investigate digital traceability infrastructure directly, but the practical value of its central finding — that prior deformation depth is the dominant predictor of reshaping outcome — is conditional on some mechanism, whether digital passport or physical re-measurement, for establishing that depth at the point of reshaping decision-making. This dependency is noted here as context for the industrial implications discussed in Chapter 4 and is not treated further in the present work.

1.10 Dimensional Tolerancing Standards and Their Relevance to Reshaped Components

A separate practical dimension of EoL reshaping feasibility, distinct from the thinning-severity focus of this thesis but directly relevant to whether a reshaped component can actually be accepted into a production assembly, is compliance with the dimensional and thickness tolerance standards that govern automotive sheet metal parts. ISO 2768 ("General tolerances"), part 2 of which addresses geometrical tolerances, and the automotive-specific VDA 2006 inspection standard both define acceptable dimensional deviation bands for stamped sheet components, though neither standard was developed with a two-step, prior-history-dependent forming process such as EoL reshaping specifically in mind.

Typical general-tolerance sheet thickness bands for automotive body panels fall in the range of ±5% to ±10% of nominal thickness for non-critical panels, tightening to ±3–5% for structural or safety-critical components where thickness directly governs load-bearing capacity (crash structures, mounting brackets). Comparing these bands against the results of this thesis is informative: the tightest baseline configuration (DN1, corner spread 0.026 mm, or ±0.8% of nominal about its own mean) would comfortably satisfy even a tight ±5% tolerance band on a per-corner basis. The most severe combined configuration (D1DN1, corner spread 0.589 mm) spans a range equivalent to roughly ±15% of nominal about its mean corner value — a spread that would fail a ±5% or even a ±10% general tolerance band if all four corners were required to fall within it, even though the least-affected individual corner (1.917 mm, 4% thinning) would itself pass comfortably in isolation.

This observation reframes the practical significance of corner-to-corner spread (defined formally in Section 2.5.2) in tolerancing terms rather than purely mechanical terms: for the most severe combined configurations identified in this thesis, the issue is not only whether the part's thinnest point remains above a fracture-safety margin (the framing used throughout Chapter 3 and Chapter 4), but also whether the part as a whole — measured at all four corners — falls within a dimensional tolerance band that a receiving assembly process would actually accept. A component that passes the fracture-safety criterion at every corner individually could still fail a uniform-thickness dimensional tolerance check if its corner-to-corner spread exceeds the applicable standard's band width, independently of the mechanical safety question. This tolerancing consideration is not pursued quantitatively further in this thesis, since it depends on the specific tolerance standard applicable to a given target component and application — information that would only be available once the reshaping framework of this thesis is applied to a specific real component (the industrial case study proposed as Priority 6 in Section 5.4) — but is noted here as a second, largely independent feasibility criterion alongside the fracture-safety criterion that has been the primary focus of Chapters 3 and 4.

1.11 Summary and Positioning of Present Work

The review establishes that: (i) direct reshaping of EoL aluminium is environmentally and economically superior to re-melting, supported by EU policy and quantitative LCA evidence; (ii) the mechanics governing reshaping outcomes are understood in principle but uncharacterised for conventional press multi-step operations; (iii) prior work focused on SPIF and hydroforming leaves conventional press reshaping unaddressed; and (iv) FEA with Johnson-Cook modelling in Abaqus/Explicit provides a validated computational framework for the forming conditions of interest. The present study addresses this gap by characterising thickness distribution across eight configurations using 2D plane strain FEA, providing the first systematic numerical dataset for conventional press-based multi-step reshaping of aluminium alloy sheet.

Chapter 2 — Methodology

2.1 Overview

The methodology comprises four components: (i) material characterisation and constitutive model specification; (ii) specimen configuration design; (iii) finite element model construction and execution; and (iv) post-processing thickness extraction. Material parameters are input to the Johnson-Cook model; the FE model geometry, boundary conditions, and contact are specified; simulations are executed for all eight configurations; nodal coordinate data is exported at the final increment; Python post-processing computes per-node thickness using the Euclidean inter-surface distance formula; and comparative analysis of thickness profiles forms the basis for Chapters 3 and 4.

2.1.1 Data Provenance and Reconstruction

A methodological note specific to this thesis is warranted. The original Abaqus output database (.odb) files for all eight simulations were lost following a hardware failure of the primary working laptop in the final weeks of this project. The results and figures presented in this thesis were reconstructed from three surviving sources: (i) screenshots of the Abaqus/CAE model tree, boundary condition manager, and interaction editor captured during model construction, two of which are reproduced as Figures 2.2 and 2.3; (ii) a CSV export of per-node thickness measurements computed at the time of the original analysis, covering all eight configurations; and (iii) the computed summary statistics (minimum thickness, thinning percentage, per-corner values, thinning gradient, corner spread) derived from that CSV and recorded in working notes prior to the hardware failure.

This reconstruction approach has two direct consequences for the content of this thesis, both already flagged in the relevant technical sections but collected here for clarity. First, the eight per-configuration thickness profile figures referenced throughout Chapter 3 (Figures 3.1–3.8) are not reproduced as finished plots in this document; the underlying numerical data survived in the CSV export, but regenerating the plots themselves — which were originally produced directly within the now-inaccessible Abaqus session and associated plotting scripts — was not possible within the time available before submission. The relevant figure positions in Chapter 3 are marked with placeholder boxes carrying the full intended caption and the summary statistics that the figure would illustrate, so that the quantitative content of each result is fully stated in the surrounding text regardless of whether the corresponding plot has been inserted. Second, model verification steps that depend on access to the live Abaqus session — mesh convergence checking and energy balance (KE/IE) monitoring, both standard practice for Abaqus/Explicit forming simulations — could not be performed retrospectively from the surviving CSV and screenshot record, since both require re-running the simulation at multiple mesh densities or inspecting time-history energy output that was not separately exported before the failure. These verification gaps are treated explicitly as limitations in Section 4.8 rather than glossed over, and are listed as the first item of future work in Section 5.4.

Two figures that depend only on the summary CSV data, rather than on regenerating Abaqus session output, were reconstructed and are included as genuine plots: Figure 3.9 (minimum thinning by configuration) and Figure 3.10 (corner spread versus thinning), both presented in Section 3.3 and generated directly from the values in Table 3.1.

2.2 Material Characterisation and Constitutive Model

The material is an AA6xxx series aluminium alloy (Al-Mg-Si) in the service-condition temper representative of an automotive body panel at end-of-life. Initial sheet thickness $t_0 = 2$ mm; elastic properties: Young's modulus E = 69 GPa, Poisson's ratio ν = 0.33, density ρ = 2700 kg/m³.

Plastic behaviour is described by the Johnson-Cook flow stress model:

$$\bar{\sigma} = (A + B\,\bar{\varepsilon}^{n})(1 + C\ln(\dot{\bar{\varepsilon}} / \dot{\bar{\varepsilon}}_0))$$

where $\bar{\sigma}$ is equivalent von Mises flow stress, $\bar{\varepsilon}$ is accumulated equivalent plastic strain, $\dot{\bar{\varepsilon}}$ is equivalent plastic strain rate, $\dot{\varepsilon}_0 = 1.0\ s^{-1}$ is the reference strain rate, A is initial yield stress [MPa], B is strain hardening modulus [MPa], n is the hardening exponent, and C is the strain rate sensitivity coefficient. The temperature-dependent term is suppressed for the isothermal quasi-static conditions of this study.

Table 2.1 — Johnson-Cook constitutive model parameters for AA6xxx series alloy.

Parameter	Symbol	Value	Unit
Initial yield stress	A	167	MPa
Strain hardening modulus	B	596	MPa
Hardening exponent	n	0.551	—
Strain rate coefficient	C	0.001	—
Reference strain rate	$\dot{\varepsilon}_0$	1.0	s^{-1}
Young's modulus	E	69,000	MPa
Poisson's ratio	ν	0.33	—
Density	ρ	2,700	kg/m³

The Johnson-Cook model was selected because: (i) it incorporates strain rate sensitivity explicitly, covering the 10^{-1} to $10^{2}\ s^{-1}$ range encountered in punch-sheet contact; (ii) it is directly implemented in Abaqus/Explicit as a built-in material model requiring no user subroutine; and (iii) calibrated parameter datasets for AA6xxx alloys are available in the published literature. For isothermal forming at the strain rates of interest, the JC isotropic hardening captures the essential monotonic flow behaviour at the accuracy level required for thickness distribution characterisation.

2.3 Specimen Configurations

Eight configurations were investigated: four baseline (single-step from virgin blanks) and four combined (two-step EoL reshaping). All share blank geometry L = 100 mm, t_0 = 2 mm. The four baseline configurations establish the reference thinning band: D1 and D2 for single-notch at 10 mm and 6 mm; DN1 and DN2 for double-notch at 8 mm and 5 mm from virgin blanks. The four combined configurations simulate EoL reshaping: blanks pre-formed to D1 or D2 condition are subjected to DN1 or DN2 second-press operations, yielding D1DN1, D1DN2, D2DN1, and D2DN2.

The combined configurations are structured as a full 2×2 factorial design over two binary variables: prior-press depth (deep, D1 = 10 mm, vs. shallow, D2 = 6 mm) and second-press depth (deep, DN1 = 8 mm, vs. shallow, DN2 = 5 mm). This factorial structure, rather than a simpler one-factor-at-a-time comparison, was adopted specifically so that the prior-depth effect and the second-press-depth effect could each be examined while holding the other constant — the comparisons exploited extensively in Chapter 3 (Section 3.3.1) and Chapter 4 (Sections 4.2–4.4). A one-factor design varying only prior depth at a single fixed second-press geometry, for instance, would not have permitted the D1DN2-vs-D2DN2 and D1DN1-vs-D2DN1 cross-comparisons that isolate the depth effect from the geometric overlap effect, nor would it have revealed the D2DN1/D2DN2 contrast (Section 4.4.1) that turned out to be the most actionable single finding of this thesis. The eight-configuration matrix is accordingly the minimum design capable of supporting the two-variable decomposition presented in the Results and Discussion chapters, given the constraint — imposed by the practical reality of manual Abaqus model setup and the available project time before the hardware failure described in Section 2.1.1 — that only two depth levels per factor were feasible within the study's scope.

Table 2.2 — All eight specimen configurations.

Config	1st Press	2nd Press	Blank Origin	EoL Scenario
D1	10 mm single	—	Virgin	Baseline: deep single notch
D2	6 mm single	—	Virgin	Baseline: shallow single notch
DN1	—	8 mm double	Virgin	Baseline: deep double notch
DN2	—	5 mm double	Virgin	Baseline: shallow double notch
D1DN1	10 mm single	8 mm double	EoL (D1)	Deep prior → deep reshape

Config	1st Press	2nd Press	Blank Origin	EoL Scenario
D1DN2	10 mm single	5 mm double	EoL (D1)	Deep prior → shallow reshape
D2DN1	6 mm single	8 mm double	EoL (D2)	Shallow prior → deep reshape
D2DN2	6 mm single	5 mm double	EoL (D2)	Shallow prior → shallow reshape

2.4 Finite Element Model

The FE model is a 2D representation (see Section 2.4.1 regarding the plane strain vs. plane stress element code discrepancy). The sheet blank is a deformable body occupying a 100 mm × 2 mm cross-section in the X-Y plane, with nominal thickness t_0 = 2 mm confirmed across all virgin-blank configurations prior to any forming operation. Punch and die are modelled as analytical rigid wires (2D line profiles) rather than as solid bodies, sketched directly as rigid wire profiles. Rigid wire tooling is an appropriate and standard idealisation for 2D Abaqus/Explicit forming models because tool deflection is negligible at the contact stresses generated in aluminium sheet forming relative to the stiffness of press-forming tool steel (E ≈ 200–210 GPa, σ_y ≈ 600–900 MPa), and a wire entity carries no independent mass or stiffness of its own, serving purely to define the rigid contact surface.

To reduce stress concentrations at the sharp corners of the rigid wire tooling profiles, a fillet of radius r = 2 mm was applied to all corner vertices of both the DN1 and DN2 die wire geometries. Figures 2.1 and 2.2 show the resulting wire profiles for the DN1 (8 mm depth) and DN2 (5 mm depth) double-notch configurations, respectively, with 135° transition angles and 20 mm pitch. The 2 mm corner fillets applied at each bend vertex are defined in the model geometry but are not visually resolved at the screenshot scale shown.

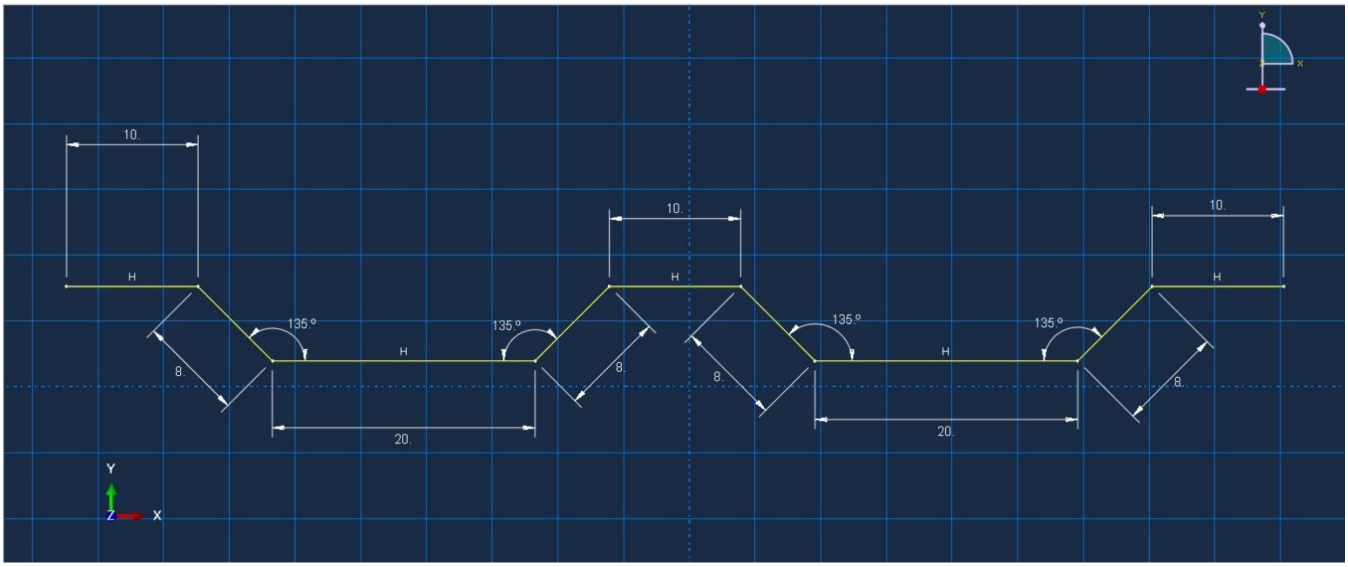

Figure 2.1 — Abaqus/CAE rigid wire profile for the DN1 double-notch die configuration (8 mm depth): 20 mm outer pitch, 10 mm inner flat, and 135° transition angles. A 2 mm corner fillet is specified in the model but not visually resolved at this scale.

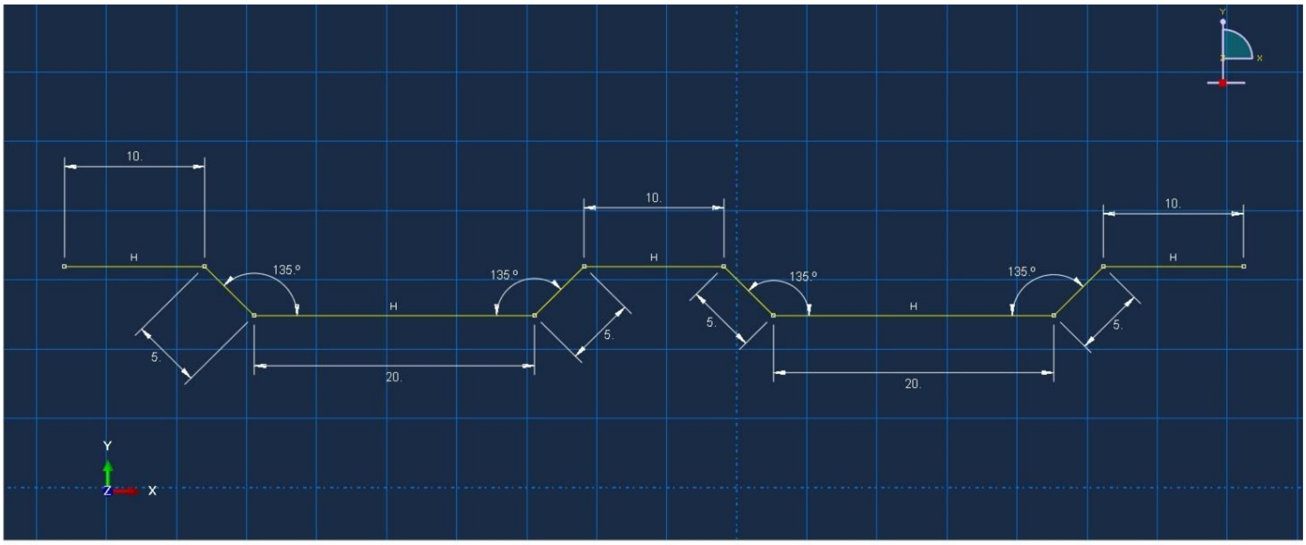

Figure 2.2 — Abaqus/CAE rigid wire profile for the DN2 double-notch die configuration (5 mm depth): same 20 mm pitch and 135° transition angles as DN1, with reduced notch depth. A 2 mm corner fillet is specified in the model but not visually resolved at this scale.

2.4.1 Element Type, Mesh, and Boundary Conditions

The blank is modelled as a deformable body; the punch and die are modelled as analytical rigid wires (2D rigid line profiles, defined as rigid wire profiles rather than as deformable or discrete rigid solid bodies, consistent with standard practice for rigid tooling in 2D Abaqus/Explicit forming models, where the tool geometry itself carries no independent stiffness and serves only to define the contact surface against which the deformable blank is formed.

The blank is meshed with 4-node reduced-integration quadrilateral elements, recorded in surviving model notes as element type CPS4R. A naming clarification is necessary here: in standard Abaqus element nomenclature, the prefix CPS denotes plane stress (Continuum Plane Stress) elements, while CPE denotes plane strain (Continuum Plane strain) elements; CPS4R is therefore conventionally a plane stress element designation, not a plane strain one. Since this thesis's analysis is described throughout as plane strain (Section 1.6.1, Section 2.4) and the surviving documentation records the element type as CPS4R, there is an internal inconsistency in the recovered model record that could not be resolved from the surviving screenshots and notes alone, given the loss of the original input file (Section 2.1.1) where the element section definition would have stated the assumption unambiguously. This discrepancy is treated as an open verification item for the model reconstruction effort (Section 5.4, Priority 0): whichever element type was in fact used, the choice carries a real mechanical consequence — plane strain elements suppress out-of-plane (width-direction) strain entirely, while plane stress elements suppress out-of-plane stress and permit free width-direction strain, and the two formulations are not mechanically equivalent for a problem (such as this one) where significant through-thickness and in-plane straining occurs at the bend corners.

The thinning results reported in Chapter 3 should therefore be read together with this caveat; the planned 3D shell extension (Section 5.4, Priority 2) would in any case resolve the question by superseding either 2D idealisation. A minimum of four elements through the 2 mm thickness provides adequate resolution of the bending strain gradient regardless of which planar formulation is ultimately confirmed.

Three boundary conditions are defined, as shown in Figure 2.3 (Abaqus Boundary Condition Manager). BC-1 constrains displacement in the X-direction (U1 = 0) at both blank ends, representing clamped press fixture ends; it is created in Step-1 (Dynamic, Explicit) and propagated through Step-2. BC-2 is applied at a reference point created for the punch and prescribes punch displacement: in Step-1 the punch reference point moves in the −Y direction to perform the forming stroke; for the combined (two-step) configurations, Step-2 prescribes the punch reference point displacement in the +Y direction, withdrawing the punch following the first forming operation rather than re-engaging the blank along the same path, consistent with a punch retraction motion between operations. BC-3 is applied to the die reference point and is released (all degrees of freedom set to zero, i.e., the die is allowed to come to rest under no externally prescribed motion) rather than held under an active prescribed displacement, reflecting the die's role as a passive forming surface rather than an actively driven tool element.

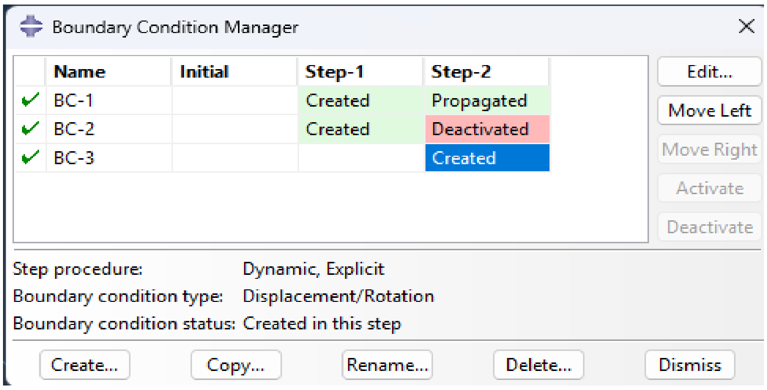

Figure 2.3 — Abaqus Boundary Condition Manager showing BC-1 (clamped ends, propagated), BC-2 (punch displacement, deactivated in Step-2), and BC-3 (die, created in Step-2). Step procedure: Dynamic, Explicit; type: Displacement/Rotation.

2.4.2 Contact Definition

Contact between the blank top surface and punch (master surface m_Surf-1) and between the blank bottom surface and die (slave surface s_Surf-1) is defined using the surface-to-surface kinematic contact method with finite sliding formulation, as shown in Figure 2.4 (Abaqus Edit Interaction dialog). The kinematic contact method enforces impenetrability through velocity corrections at the contact interface, providing robust performance during large-deformation bending at punch corners. Friction is modelled using the isotropic Coulomb law with coefficient μ = 0.1, representative of a lubricated aluminium-on-steel tooling interface.

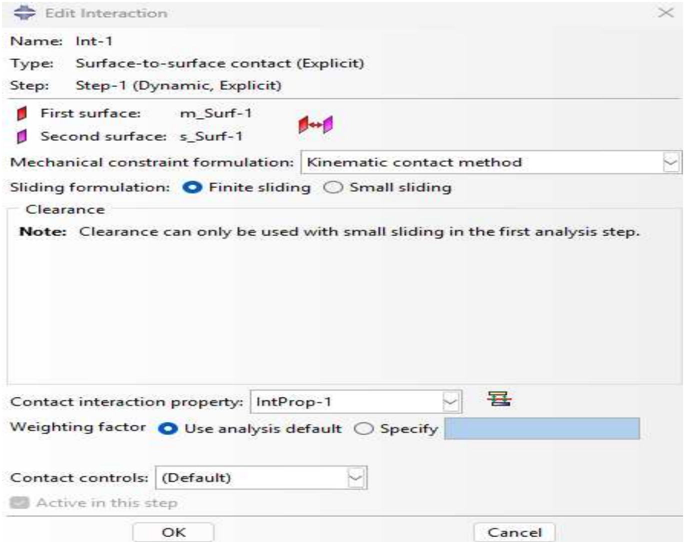

Figure 2.4 — Abaqus Edit Interaction dialog: surface-to-surface contact (Explicit), kinematic constraint formulation, finite sliding, contact property IntProp-1. Master surface m_Surf-1 (punch), slave surface s_Surf-1 (blank).

2.4.3 Mesh Density

The blank mesh uses a global seed size of 0.25 mm, providing approximately 800 elements along the blank length and 4 elements through the 2 mm thickness — sufficient resolution of the through-thickness bending strain gradient, which varies quadratically across the cross-section under pure bending. A formal mesh convergence study (comparing coarse, medium, and fine mesh predictions) was not performed for this thesis due to the loss of the original Abaqus model files; the single mesh density reported here was reconstructed from saved screenshots, output CSV data, and notes following a hardware failure. This is acknowledged as a methodological limitation in Section 4.8 and identified as a priority validation step in future work (Section 5.4).

Table 2.3 — Abaqus/Explicit model settings summary.

Parameter	Value / Setting
Element type	CPS4R per surviving notes (see Section 2.4.1 — plane stress/strain code discrepancy unresolved)
Blank dimensions	100 mm × 2 mm (L × t_0)
Global mesh seed	0.25 mm (single density used; not convergence-tested)
Through-thickness elements	4 minimum
Punch/die	Analytical rigid body
Contact formulation	Surface-to-surface, kinematic, finite sliding
Friction coefficient μ	0.10 (Coulomb, lubricated Al-steel)
Time integration	Central difference (explicit)
Mass scaling	Not formally verified (KE/IE not monitored — model files lost)
Constitutive model	Johnson-Cook isotropic hardening (isothermal)
Step type	Dynamic, Explicit

2.4.4 Representative Deformed Shape and Stress State

The Abaqus/CAE analysis produced deformed-shape outputs at the final forming increment for each configuration, capturing the notch geometry pressed into the sheet and the resulting local bending at punch corners. These outputs — shown per-configuration in Chapter 3 immediately following each thickness profile — provide a qualitative visual cross-check: regions of concentrated local bending correspond spatially to the corner thinning minima identified in the numerical thickness profiles. Stress localisation is visible in the contour shading, though the original colour-scale calibration was not recovered following the hardware failure described in Section 2.1.1; accordingly these images are presented as qualitative geometry checks rather than quantitative stress results.

A note on the extraction procedure: thickness was computed in post-processing from deformed nodal coordinates using the Euclidean inter-surface distance formula described in Section 2.5, applied to paired top-surface and bottom-surface node sets at equivalent parametric positions along the sheet arc length.

Energy balance monitoring (the ratio of kinetic to internal energy, KE/IE) is the standard diagnostic for confirming quasi-static validity in mass-scaled Abaqus/Explicit simulations, and would normally be reported here. Following the loss of the original Abaqus output database files (.odb) to a hardware failure during the final stage of this work, this diagnostic could not be re-extracted; only the screenshot record, the thickness CSV, and computed results survived. The absence of formal energy balance verification is acknowledged as a limitation in Section 4.8 and is the first item recommended for re-verification once the simulations are reconstructed (Section 5.4, Priority 0).

2.5 Thickness Extraction and Post-Processing

Abaqus/Explicit does not provide a direct nodal thickness output for CPS4R plane strain elements (unlike S4R shell elements, which output STH directly). Thickness was therefore computed in post-processing from deformed nodal coordinates exported from Abaqus at the final increment for two node sets — top surface (TOP_SURF) and bottom surface (BOT_SURF) — each containing approximately 200 nodes per configuration, spanning the full 100 mm nominal blank length (the deformed arc length differs slightly from 100 mm due to forming-induced stretching, typically reaching 101–105 mm depending on configuration severity).

2.5.1 Two Incorrect Methods and the Correct Nearest-Neighbour Approach

Two superficially reasonable thickness extraction formulas were evaluated during this work and found to be unsuitable, and identifying why is itself informative for anyone reproducing this methodology. The first candidate formula uses only the vertical (Y) coordinate difference between same-index top and bottom nodes, $t_i = |Y_{top,i} - Y_{bot,i}|$. This is correct only where the sheet is locally horizontal; at the inclined sidewalls of a notch — where the local surface normal departs substantially from vertical — the true thickness is measured perpendicular to the local surface, not vertically, and the vertical-difference formula systematically overestimates the true strain-induced thinning, in some regions by a large margin. Applied to the present dataset, this Y-difference formula returns implausibly low values (down to roughly 0.6 mm, i.e., approximately 70% thinning) at exactly the steep sidewall regions where the geometric distortion between vertical and true-normal measurement is largest — physically excessive thinning that is inconsistent with the absence of any fracture indicator in the simulation and is an artefact of the formula, not the underlying mechanics.

The second candidate formula computes the same-index Euclidean distance, $t_i = \sqrt{(X_{top,i} - X_{bot,i})^2 + (Y_{top,i} - Y_{bot,i})^2}$, pairing the i-th top node with the i-th bottom node by list index. This is an improvement over the Y-only formula in flat and mildly curved regions, but fails wherever the top and bottom node sets are not seeded with exactly corresponding parametric positions along their respective arc lengths — which, for the present mesh, was not guaranteed because the top and bottom surfaces deform by different amounts during forming (the surface in contact with the punch follows a different stretch path than the surface in contact with the die) and node numbering was assigned independently for the two surfaces during the original mesh generation. Where the two index sequences drift out of true geometric correspondence, the same-index Euclidean formula instead measures the distance between two nodes that are not actually opposite one another through the sheet thickness, and the result is essentially noise — in this study, the same-index formula produced spuriously inflated thickness values exceeding the nominal 2.0 mm at exactly the corners where index drift is largest, the opposite failure mode from the Y-only formula.

The correct method, used to produce all thickness values, profiles, and statistics reported in this thesis, is a nearest-neighbour Euclidean mapping: for each top-surface node i at position $(X_{top,i}, Y_{top,i})$, the true local thickness is taken as the minimum Euclidean distance to any node on the bottom-surface node set, $t_i = \min_j \sqrt{(X_{top,i} - X_{bot,j})^2 + (Y_{top,i} - Y_{bot,j})^2}$, evaluated over all bottom-surface nodes j rather than only the same-index node. This correctly identifies the actual nearest point on the opposite surface regardless of how the two surfaces' node numbering may have drifted relative to one another, and is geometrically the appropriate definition of local sheet thickness — the shortest distance from a point on one surface to the opposite surface — under the moderate curvature conditions present in this study's bend-corner geometry. This nearest-neighbour computation was implemented in Python, reading the exported nodal coordinate CSV and computing, for every top node, the minimum distance to the full bottom node set.

Validation: applying the nearest-neighbour method to all eight configurations returns 1.998–2.007 mm (within ±0.4% of t_0 = 2.0 mm) in flat, undeformed blank regions away from any notch, confirming extraction accuracy at the locations where the true answer is known by construction. The minimum thickness values obtained by this method are reported throughout Chapter 3 and are, by construction, never able to exceed the nominal 2.0 mm — unlike the flawed same-index Euclidean formula — since the nearest-neighbour distance to a real opposite-surface node cannot exceed the local sheet thickness by definition, other than the very small numerical noise visible in a handful of nodes (≤0.04 mm above nominal) attributable to mesh node spacing rather than a thickness-computation error.

2.5.2 Derived Metrics: Definitions

Four derived metrics are computed from the per-node thickness profile t(x) for each configuration and used throughout Chapter 3. Their precise definitions are given here to avoid ambiguity in later discussion.

Minimum thickness (t_min) is simply the lowest value of t_i across all nodes in the profile — the single most-thinned point on the entire sheet for that configuration. Thinning percentage is computed as $100 \times (1 - t\_min/t_0)$, expressing the minimum thickness as a percentage reduction from the nominal 2.0 mm starting thickness.

Per-corner minimum is the local minimum thickness value at each individual bend corner considered separately, rather than the single global minimum across the whole sheet. A single-notch configuration (D1, D2) has two corners (one on each side of the notch); a double-notch or combined configuration has four. Corner minima are identified in this thesis using a peak-detection algorithm applied to the thickness profile, locating each local dip below a threshold value and reading off the true minimum within that local dip. The global minimum thickness reported for a configuration (t_min above) is simply the smallest of that configuration's corner minima.

Corner-to-corner spread — the metric most central to the quality-control discussion in Section 3.3.3 — is defined as the difference between the largest and smallest corner minimum within a single configuration: spread = max(corner minima) − min(corner minima). This is a within-configuration measure of non-uniformity, distinct from thinning percentage, which is a measure of severity. A configuration can have severe thinning (low t_{min}) but low spread, if every corner thins by approximately the same amount (DN1 is an example: t_{min} = 1.633 mm, but all four corners sit within 0.026 mm of each other). Conversely, a configuration can have a smaller drop in its worst corner but a much larger spread, if some corners are barely affected while others are severely thinned (D2DN2 illustrates this contrast with DN1: comparable overall severity, but a corner spread more than nine times larger).

Physically, low spread indicates that the forming operation treats every corner of the tooling approximately equally — the outcome at any one corner is representative of the whole part, and a single-point thickness measurement taken at manufacturing quality control would give a trustworthy picture of the part's condition. High spread indicates that different corners of the same forming operation are experiencing meaningfully different local conditions — most often, in the combined configurations of this thesis, because some corners of the second-press tooling happen to land on blank material that carries heavy strain history from the first press, while other corners land on material that the first press left largely undisturbed. In that situation, a single-point measurement is unreliable: measuring the "lucky" corner would understate the part's true condition, while measuring the "unlucky" corner would overstate it relative to the rest of the part. This is why Section 3.3.3 argues that combined (two-step) EoL configurations specifically require multi-point corner-by-corner thickness inspection rather than a single spot check, and why corner spread — not just minimum thickness — is tracked as an independent metric throughout Chapter 3 rather than being treated as a secondary detail of the minimum-thickness result.

Maximum thinning gradient is the largest absolute change in thickness between adjacent nodes along the arc-length profile, $\max_i |t_{i+1} - t_i|$, reported in units of mm per node interval. This captures how abruptly the profile drops toward its minimum, independently of how low that minimum actually is: a steep gradient means the thinnest point is reached over a short spatial distance (a sharp, narrow dip in the profile), while a shallow gradient means the same minimum is approached more gradually over a wider region. A sharp, spatially concentrated thin zone is generally considered a more severe condition from a fracture-initiation standpoint than the same minimum thickness spread over a broader area, since strain concentration itself (independent of the absolute strain level) is a recognised driver of localised necking in sheet metal — this is the physical justification for tracking gradient as a metric distinct from minimum thickness, discussed further in Section 3.3.2.

Chapter 3 — Results

This chapter presents thickness distribution results for all eight configurations. Section 3.1 covers the four baseline configurations; Section 3.2 covers the four combined EoL configurations; Section 3.3 presents multi-metric comparative analysis. For each configuration, the minimum thickness, thinning percentage, per-corner minima, maximum thinning gradient, and spatial characteristics are reported.

3.1 Baseline Configurations

3.1.1 D1 — Single Notch, 10 mm Depth, Virgin Blank

D1 represents single-step forming to 10 mm notch depth from a virgin blank. The thickness profile exhibits two thinning events at the left and right bend corners (single-notch tooling produces exactly two corners, not four; the geometry has no second notch). Flat regions recover to the nominal 2.0 mm, confirming spatially localised thinning.

Minimum thickness: 1.620 mm (19.0% thinning). The two corner minima are 1.642 and 1.626 mm — a spread of only 0.017 mm, indicating excellent symmetry consistent with symmetric single-notch tooling. Maximum thinning gradient: 0.206 mm/node.

Applying the strain-path reasoning of Section 1.4.1, the predicted thickness strain at this thinning level is $\varepsilon_3 = \ln(1.620/2.000) \approx -0.210$, implying a major in-plane strain $\varepsilon_1 \approx +0.210$ under the plane strain assumption $\varepsilon_1 = -\varepsilon_3$. This places the D1 corner state at a major strain within the published plane strain FLC range for 6xxx in T4 temper (0.15–0.25, Section 1.4.2) and modestly above the more conservative T6 minimum (0.10–0.18) — the latter being the more relevant bound given the EoL service condition assumed for this study, and the comparison underscores that even the mildest baseline configuration is not negligibly far from the empirical necking boundary once the more conservative T6 FLC estimate is used, though no necking or fracture indicator was observed in the simulation itself. The D1 baseline nonetheless retains meaningfully more strain margin than the combined configurations examined in Section 3.2, and serves as a low-severity reference point for that comparison.

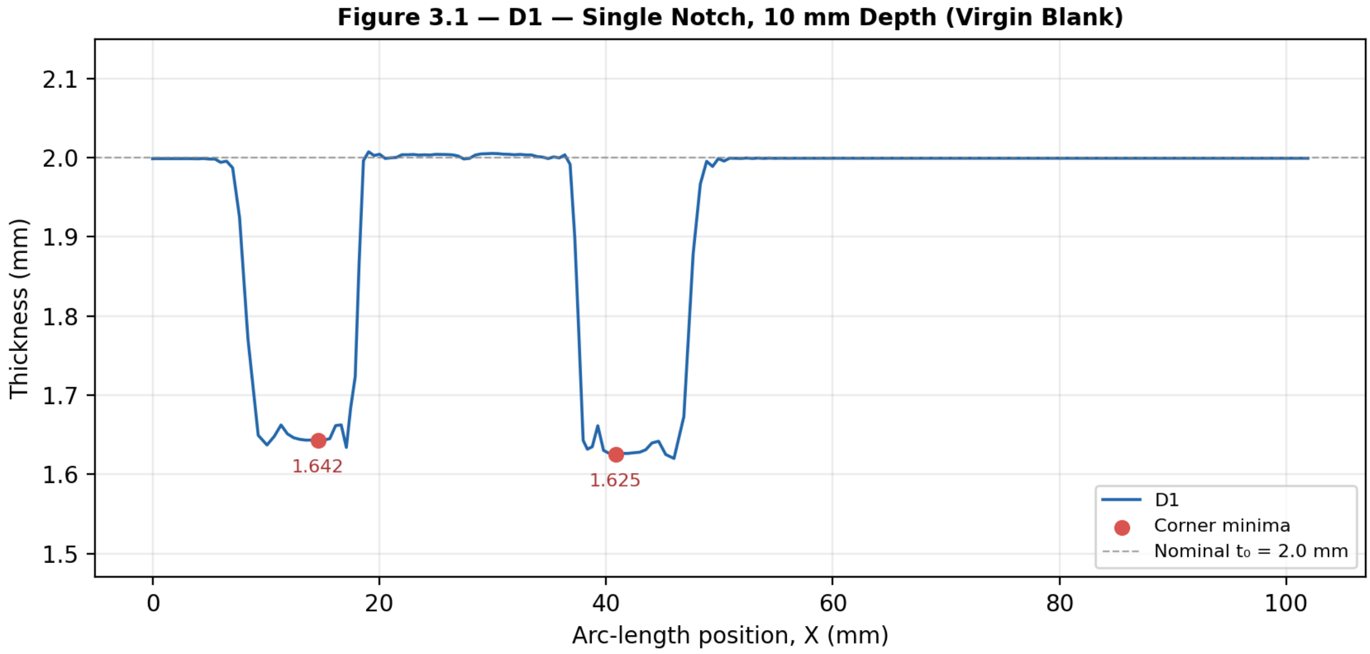

Figure 3.1 — D1 (10 mm single notch, virgin blank): thickness profile vs. arc-length position, computed by nearest-neighbour Euclidean mapping (Section 2.5.1). Two symmetric corner thinning events; min t = 1.620 mm (19.0%).

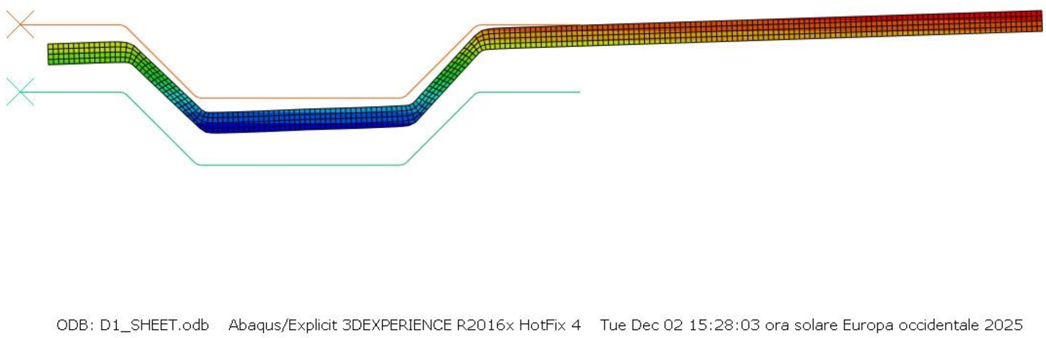

Figure 3.1b — D1 (10 mm single notch, virgin blank): deformed blank shape at the final forming increment. Contour shading indicates relative deformation magnitude; colour scale not recovered (qualitative reference).

3.1.2 D2 — Single Notch, 6 mm Depth, Virgin Blank

D2 represents single-step forming to 6 mm depth from a virgin blank. Minimum thickness: 1.595 mm (20.2% thinning) — somewhat more severe than D1 despite the reduced depth. This counterintuitive result reflects local corner geometry: a shallower notch with the same punch radius creates a more abrupt angular transition, concentrating bending strain more locally. The r/t ratio (punch radius to sheet thickness), not notch depth, is the dominant parameter governing peak corner thinning in single-step forming within this range.

The two corner minima are 1.595 and 1.651 mm — a spread of 0.056 mm, more than three times the D1 spread (0.017 mm) despite D2 being nominally as symmetric a single-notch geometry as D1. Maximum thinning gradient: 0.169 mm/node, lower than D1's 0.206 mm/node even though D2's minimum thickness is lower — indicating that D2's thinning, while reaching a slightly lower absolute value, develops more gradually along the arc length than D1's.

The corresponding major strain estimate is $\varepsilon_1 \approx +0.226$, marginally higher than D1 and consistent with the FLC comparison discussed in Section 3.1.1. The larger corner spread relative to D1 is notable given the nominal symmetry of both single-notch geometries; this likely reflects greater sensitivity of the shallower, more acute corner geometry to small asymmetries in the discretised die profile (Figure 2.1) or in punch-die alignment, an effect that would be straightforward to confirm or rule out once the model is reconstructed (Section 5.4, Priority 0). Since D2 (20.2% thinning) is the single most severe baseline configuration despite its shallow depth, it consumes the largest share of the T6 FLC margin among the four baseline cases — a further practical argument, alongside the general r/t-dominance finding, for basing tooling and process risk assessment on measured corner severity rather than on notch depth as a proxy.

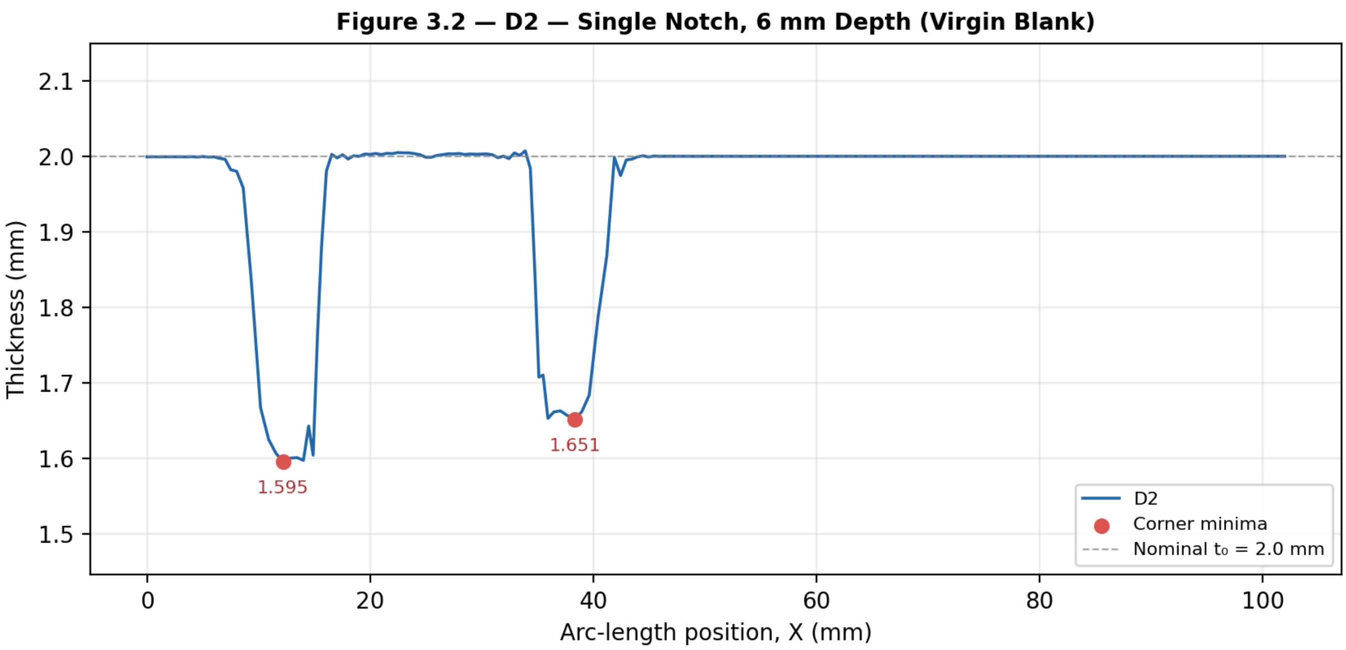

Figure 3.2 — D2 (6 mm single notch, virgin blank): thickness profile vs. arc-length position. Two corner thinning events; min t = 1.595 mm (20.2%), the most severe of the four baseline configurations.

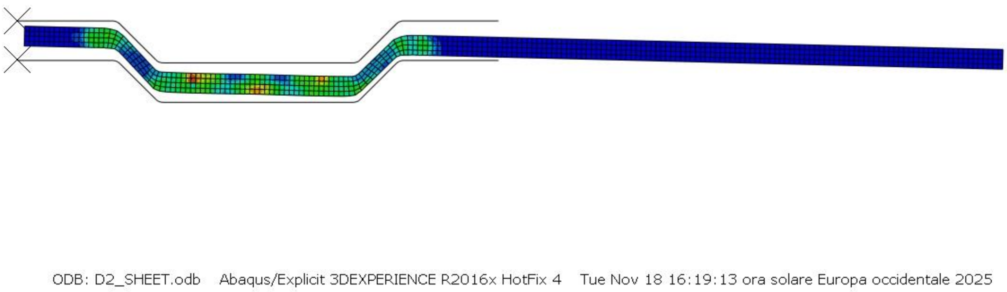

Figure 3.2b — D2 (6 mm single notch, virgin blank): deformed blank shape at the final forming increment. Contour shading qualitative.

3.1.3 DN1 — Double Notch, 8 mm Depth, Virgin Blank

DN1 involves simultaneous pressing of two notches to 8 mm depth from a virgin blank. The profile exhibits four thinning events — two per notch — with a flat plateau between the notches recovering to nominal thickness. This confirms the absence of interaction between the two deformation zones.

Minimum thickness: 1.633 mm (18.4% thinning). The four corner minima are 1.638, 1.639, 1.632, and 1.658 mm — a spread of only 0.026 mm, the most uniform of any configuration in the study. This exceptional uniformity reflects simultaneous symmetric pressing of both notches, distributing forming load evenly across all four corners. Maximum thinning gradient: 0.164 mm/node, the lowest of any configuration. DN1 serves as the primary reference for D1DN1 and D2DN1 comparison, enabling isolation of the prior deformation effect.

That DN1's minimum thickness (1.633 mm) falls close to D1 (1.620 mm) and between the single-notch baselines is broadly consistent with the r/t-dominance argument of Section 3.1.2, though the four baseline configurations do not interpolate as cleanly by depth alone as a simple monotonic relationship would suggest — D2 (the shallowest single-notch depth, 6 mm) in fact produces the single most severe baseline minimum (1.595 mm), not D1 or DN2. This reinforces that local corner angle and r/t ratio, rather than depth, are the first-order drivers within the baseline group, and that depth-based intuition alone is an unreliable predictor of relative severity even among configurations using virgin blanks and the same general tooling family.

In FLC terms, DN1's minimum thickness corresponds to a major strain estimate of $\varepsilon_1 \approx \ln(2.000/1.633) \approx +0.202$, close to D1's estimate and, like D1, positioned at the upper edge of the T6 plane strain FLC range (0.10–0.18) rather than comfortably within it — a reminder that even the most uniform baseline configuration in this study is not far, in strain-path terms, from the empirical necking boundary, notwithstanding the absence of any fracture indicator in the simulation itself.

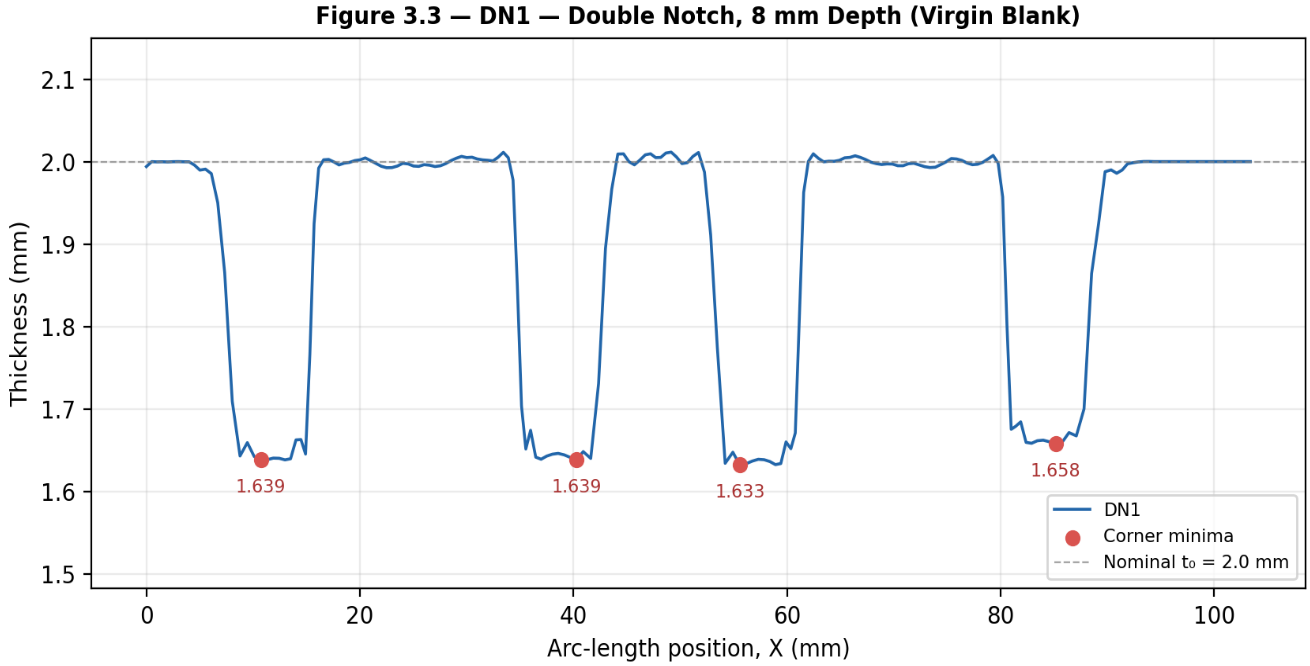

Figure 3.3 — DN1 (8 mm double notch, virgin blank): thickness profile vs. arc-length position. Four symmetric corner thinning events; min t = 1.633 mm (18.4%), spread 0.026 mm — most uniform baseline.

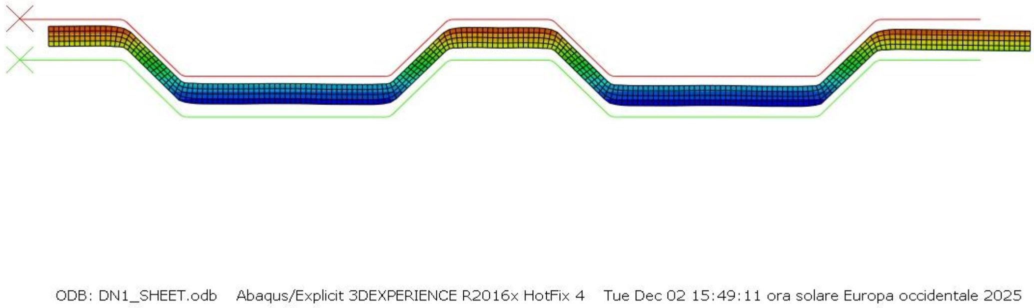

Figure 3.3b — DN1 (8 mm double notch, virgin blank): deformed blank shape at the final forming increment. Contour shading qualitative.

3.1.4 DN2 — Double Notch, 5 mm Depth, Virgin Blank

DN2 involves simultaneous pressing of two notches to 5 mm depth from a virgin blank. Minimum thickness: 1.622 mm (18.9% thinning). The four corner minima are 1.645, 1.682, 1.622, and 1.717 mm — a spread of 0.095 mm, the largest spread among the four baseline configurations and roughly 3.7 times the DN1 spread (0.026 mm) despite both using the same double-notch tooling family at different depths. Maximum thinning gradient: 0.217 mm/node.

The larger corner spread in DN2 relative to DN1, despite both sharing the double-notch geometry, suggests that the shallower 5 mm depth makes the resulting corner severity more sensitive to small differences between the two nominally identical notch positions than the deeper 8 mm DN1 geometry — broadly the same r/t-sensitivity argument already used to explain the D1/D2 comparison in Section 3.1.2, here appearing as inter-notch spread rather than as a comparison between independent configurations.

The four baseline configurations together cluster within an 18.4–20.2% thinning band — a range of only 1.8 percentage points — across the full range of notch depths (5–10 mm) and both single and double notch geometries. This tight clustering is itself a key finding: for single-step forming from virgin blanks, thinning severity is dominated by the punch radius-to-thickness ratio (r/t) and local corner angle rather than by notch depth or single-vs-double tooling family. This provides a robust, low-scatter reference band against which the substantially elevated combined-configuration thinning in Section 3.2 is quantified.

DN2's major strain estimate, $\varepsilon_1 \approx \ln(2.000/1.622) \approx +0.209$, is essentially indistinguishable from DN1's (+0.202) despite the difference in double-notch depth (5 mm vs. 8 mm) — a further confirmation, alongside the D1/D2 and DN1/DN2 near-equivalence already noted, that depth alone is a weak predictor of strain-path severity for the geometry family investigated in this study, with local corner radius and included angle mattering considerably more.

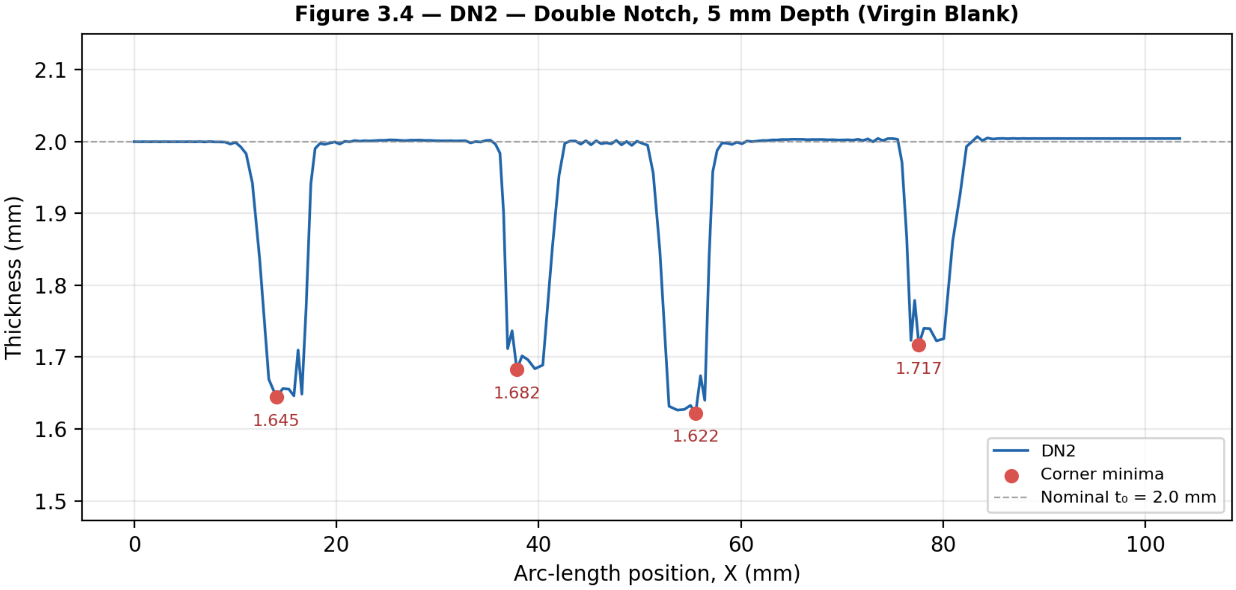

Figure 3.4 — DN2 (5 mm double notch, virgin blank): thickness profile vs. arc-length position. Four corner thinning events; min t = 1.622 mm (18.9%), spread 0.095 mm — largest baseline spread.

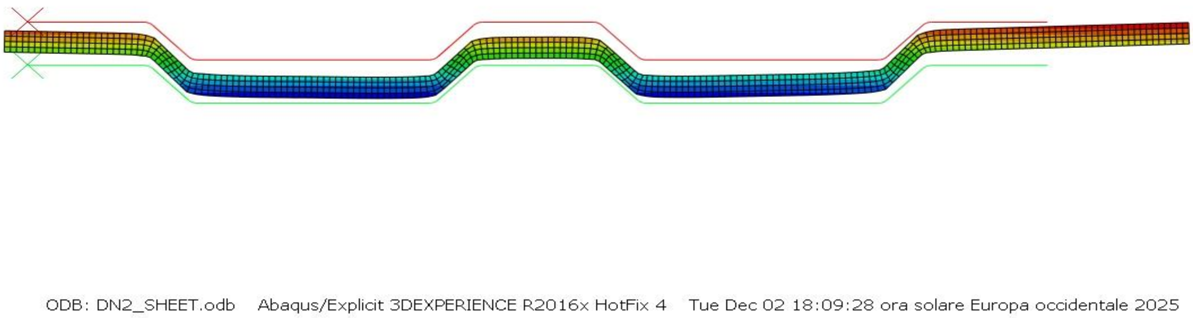

Figure 3.4b — DN2 (5 mm double notch, virgin blank): deformed blank shape at the final forming increment. Contour shading qualitative.

3.2 Combined EoL Configurations

The combined configurations represent the scientific core of this study. Blanks first pressed to D1 or D2 single-notch geometry are subsequently subjected to a second press operation with DN1 or DN2 double-notch tooling. The second press targets a different region of the blank from the first, simulating an industrial reshaping operation where a new part geometry is pressed into a blank retaining the geometry and deformation history of its EoL condition.

3.2.1 D1DN1 — 10 mm Single then 8 mm Double

D1DN1 is the most severe combined configuration. The D1 first press deposits the highest prior strain of any first-press operation (PEEQ ≈ 18–20% at corners). The DN1 second press then engages this pre-damaged blank.

Minimum thickness: 1.328 mm (33.6% thinning). The DN1 virgin baseline is 1.633 mm (18.4%). Additional thinning attributable to prior deformation: 15.2 percentage points. The four corner minima are 1.409, 1.542, 1.328, and 1.917 mm — a spread of 0.589 mm, roughly twenty-three times the DN1 baseline spread of 0.026 mm. The critical corner (1.328 mm) occurs where the second-press deformation zone spatially overlaps with the first-press deformation zone, concentrating cumulative PEEQ from both operations. Maximum thinning gradient: 0.375 mm/node, more than double the baseline range (0.164–0.217 mm/node) — indicating a steeper, more localised approach to minimum thickness and heightened spatial concentration of damage.

Using the same strain-path estimate as Section 3.1.1, the critical corner's major strain is $\varepsilon_1 \approx \ln(2.000/1.328) \approx +0.410$ if the full thinning were attributed to a single monotonic strain path from virgin condition. In reality this strain accrued in two increments — the D1 first-press contribution and the DN1 second-press contribution — and the two increments are not necessarily co-directional in the principal strain frame, given the differing notch geometry and corner orientation between the D1 and DN1 tooling. Nonetheless, the total accumulated major strain at this corner is comfortably above the T6 plane strain FLC range (0.10–0.18, Section 1.4.2) quoted for the virgin-blank case, indicating that — unlike D1 considered in isolation — the D1DN1 critical corner has likely crossed into a strain regime where the empirical FLC would predict elevated necking risk, even though the explicit FE simulation itself did not report element deletion or other direct fracture indicators. This is the clearest single piece of evidence in this thesis that D1DN1 should be treated as the marginal case described in Section 3.3.4, and reinforces the recommendation in Section 4.9 that this configuration class proceed only with full corner-level thickness verification.

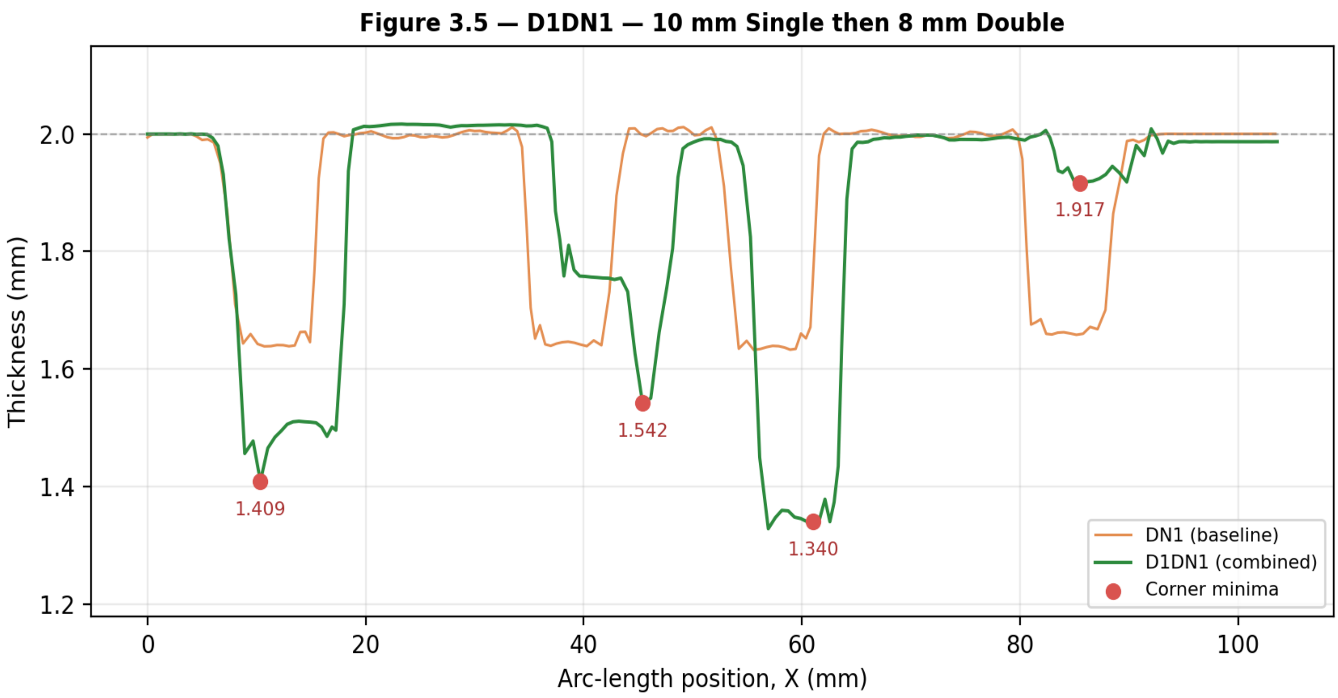

Figure 3.5 — D1DN1 (green) vs. DN1 baseline (orange): 15.2 pp additional thinning; corner spread ≈22× baseline. Critical minimum t = 1.328 mm (33.6%) at geometric overlap corner.

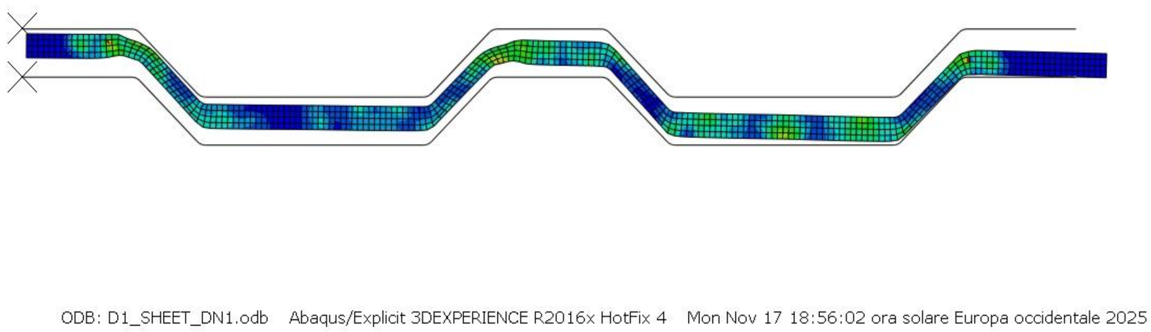

Figure 3.5b — D1DN1 (10 mm single then 8 mm double): deformed blank shape at the final forming increment. Contour shading qualitative.

3.2.2 D1DN2 — 10 mm Single then 5 mm Double

D1DN2 represents a deep first press (D1: 10 mm) followed by a shallower second press (DN2: 5 mm). Minimum thickness: 1.442 mm (27.9% thinning) — 9.0 pp above the DN2 baseline (18.9%). Although less severe than D1DN1, this remains well above the baseline band, confirming that deep prior deformation elevates thinning regardless of second-press depth within the ranges investigated.

The four corner minima are 1.442, 1.453, 1.560, and 1.930 mm — a spread of 0.487 mm. Maximum gradient: 0.263 mm/node. The 1.930 mm corner is close to nominal, indicating that — as in D1DN1 — the second-press tooling engages some corners that were essentially undisturbed by the first press and others that inherit substantial prior strain, with the spread of outcomes spanning nearly the full range between near-baseline and the configuration minimum.

The comparison between D1DN1 (deep prior + deep second press, 33.6%) and D1DN2 (deep prior + shallow second press, 27.9%) isolates the effect of second-press severity given a fixed, severe prior history: reducing the second-press depth from 8 mm to 5 mm recovers 5.7 percentage points of thinning margin even though the prior D1 deformation is identical in both cases. This is a directly actionable observation for process design: where a deep-history EoL blank must be reshaped and the target geometry permits some flexibility in forming depth, reducing second-press severity is an effective lever for managing thinning risk, complementing the corner-position and depth-sorting interventions discussed in Section 4.9.

The critical corner's major strain estimate for D1DN2 is $\varepsilon_1 \approx \ln(2.000/1.442) \approx +0.328$, comfortably above the T6 FLC range and roughly 60% higher than the DN2 baseline estimate (+0.209) — a smaller strain-path elevation than D1DN1's (+0.410 vs. DN1's +0.202, more than double), consistent with D1DN2 occupying an intermediate severity position between the near-baseline D2DN1 and the marginal D1DN1 across every metric examined in this thesis.

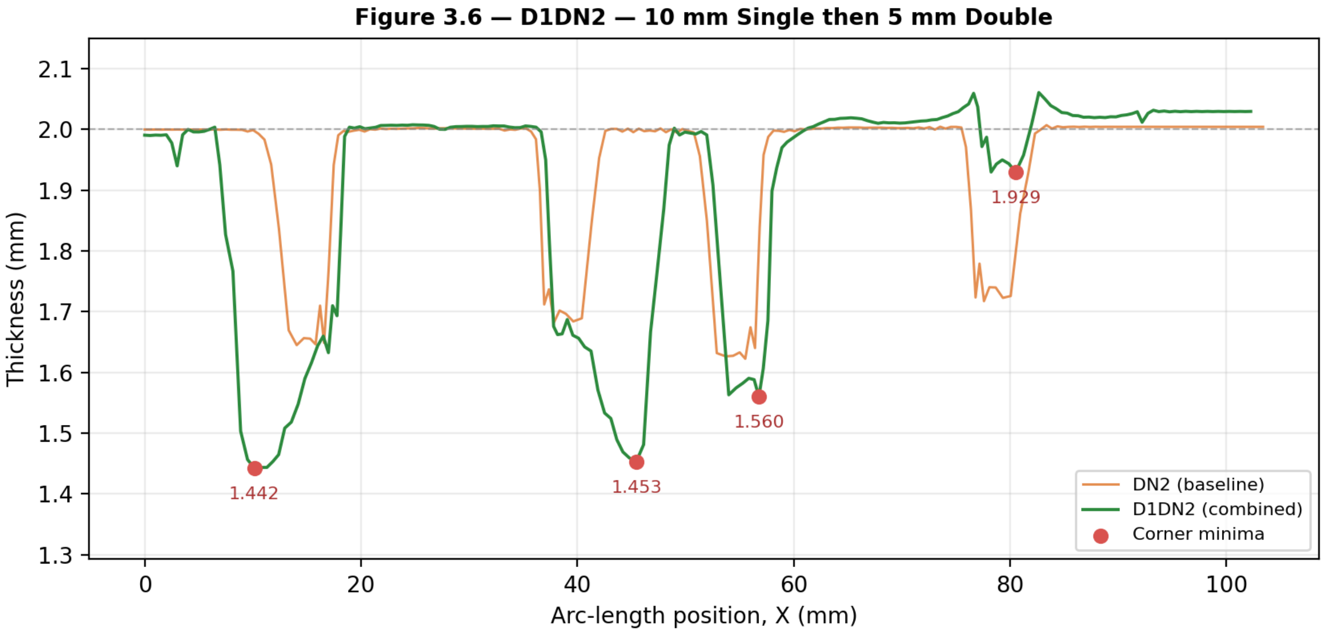

Figure 3.6 — D1DN2 (green) vs. DN2 baseline (orange): min t = 1.442 mm (27.9%), 9.0 pp above baseline. Corner spread 0.487 mm spans near-baseline to critical.

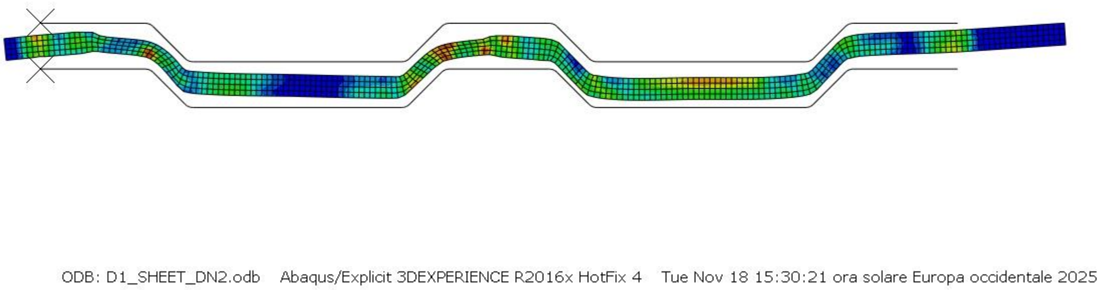

Figure 3.6b — D1DN2 (10 mm single then 5 mm double): deformed blank shape at the final forming increment. Contour shading qualitative.

3.2.3 D2DN1 — 6 mm Single then 8 mm Double

D2DN1 contains the most practically significant finding of this study. The D2 first press (6 mm, PEEQ ≈ 10–12% at corners) is the shallowest prior operation. Minimum thickness: 1.611 mm (19.5% thinning) — only 1.1 percentage points above the DN1 baseline of 18.4% (1.633 mm).

This near-zero difference means a blank previously formed to a 6 mm shallow single-notch depth behaves almost indistinguishably from a virgin blank in the subsequent 8 mm double-notch reshaping. The shallow first press raised local yield stress but consumed insufficient ductility to meaningfully degrade second-operation formability. The four corner minima are 1.611, 1.615, 1.618, and 1.633 mm — spread of only 0.022 mm, slightly tighter even than the DN1 baseline spread (0.026 mm). Maximum gradient: 0.216 mm/node, within the baseline range. All four metrics converge on a near-baseline outcome, providing robust evidence that shallow prior deformation does not compromise reshaping feasibility.

It is worth noting explicitly that D2DN1 uses the deeper of the two second-press geometries (DN1, 8 mm) paired with the shallower of the two first-press geometries (D2, 6 mm) — in other words, this is not a case where both operations happen to be mild. The second-press severity is comparable to that in D1DN1, yet the outcome is close to baseline. This strengthens the conclusion that prior-press depth, not second-press depth, is the dominant variable distinguishing the favourable D2-based combined configurations from the unfavourable D1-based ones, at least for the depth range and geometries investigated in this study.

D2DN1's major strain estimate, $\varepsilon_1 \approx \ln(2.000/1.611) \approx +0.216$, sits essentially on top of the DN1 baseline estimate (+0.202) — a strain-path confirmation of the near-zero severity elevation already established through the minimum-thickness and corner-spread metrics, and the strongest evidence in this thesis that a 6 mm prior press genuinely does not measurably erode residual formability for a subsequent 8 mm double-notch operation.

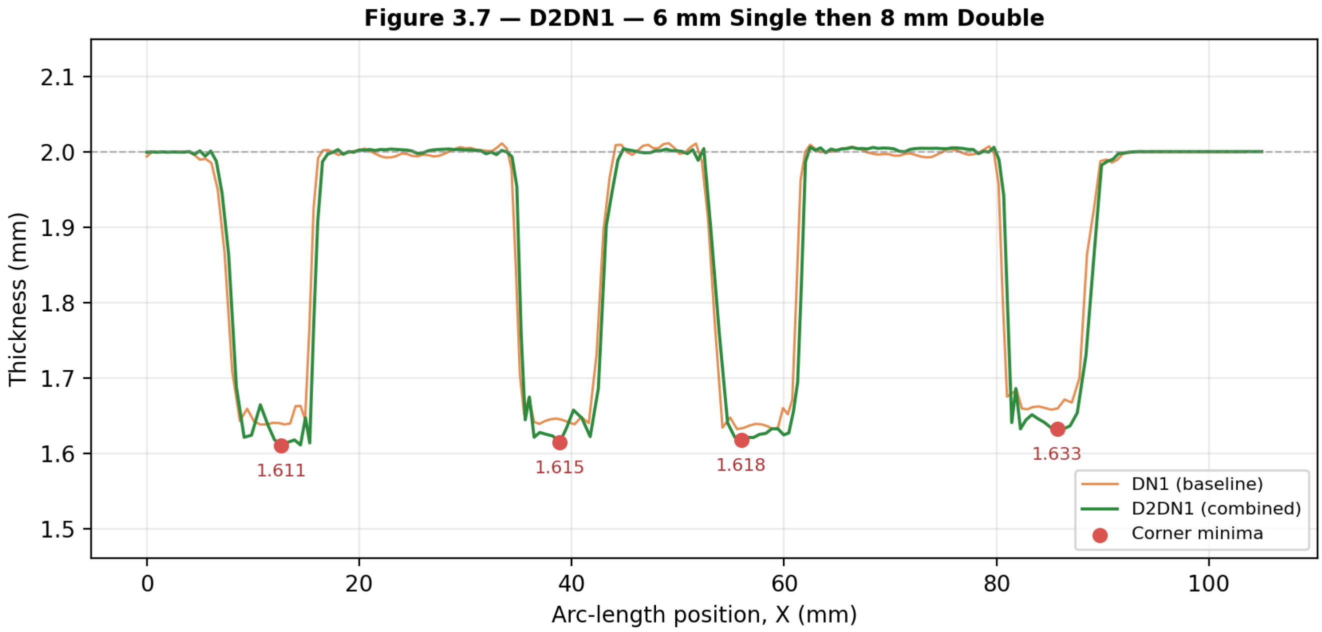

Figure 3.7 — D2DN1 (green) vs. DN1 baseline (orange): near-identical profiles confirm negligible effect of 6 mm shallow prior history. Min t = 1.611 mm (19.5%). Most favourable EoL configuration; tightest corner spread (0.022 mm) of any combined configuration.

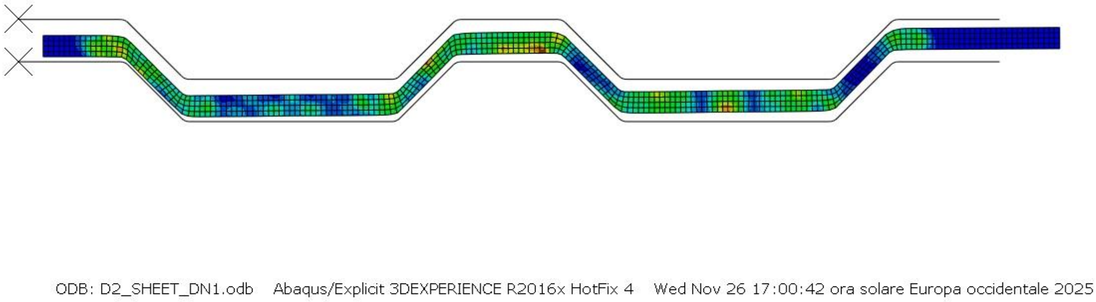

Figure 3.7b — D2DN1 (6 mm single then 8 mm double): deformed blank shape at the final forming increment. Contour shading qualitative.

3.2.4 D2DN2 — 6 mm Single then 5 mm Double

D2DN2 produces the second-most severe thinning (28.3%, 1.433 mm minimum) despite using shallower operations than D1DN1 on both the first and second press. This result is the most mechanistically complex in the dataset.

The prior D2 first press is identical to D2DN1 (6 mm, PEEQ ≈ 10–12%). Yet D2DN2 produces 28.3% versus D2DN1's 19.5% — an 8.8 pp difference attributable entirely to second-press geometry and spatial corner alignment. For the D2 + DN2 combination, the corner positions of the two operations partially overlap along the blank length: the DN2 second press engages material already locally thinned by the D2 first press. The four corner minima are 1.508, 1.581, 1.433, and 1.686 mm — a spread of 0.253 mm, smaller than D1DN1's spread (0.589 mm) but still roughly ten times the favourable D2DN1 spread (0.022 mm), with the heavily thinned overlap corner (1.433 mm) sitting well below the other three. Geometric corner overlap is thus an independent damage amplification mechanism, operating independently of absolute forming depths.

The pairing of D2DN1 (near-baseline) and D2DN2 (second-worst in the dataset), both sharing the identical D2 prior press, is the cleanest possible isolation of the geometric overlap mechanism from the prior-depth mechanism available within this study's eight-configuration matrix: with prior history held constant, the outcome swings by 8.8 percentage points purely as a function of second-press tooling geometry and its resulting corner alignment relative to the first press. This single comparison is arguably the most actionable finding in the entire dataset for an industrial process engineer, since corner-position planning (Section 4.9) is a tooling and fixturing decision rather than a material or design constraint, and is therefore the lowest-cost intervention identified anywhere in this thesis.

D2DN2's overlap-corner major strain estimate, $\varepsilon_1 \approx \ln(2.000/1.433) \approx +0.334$, is close to D1DN2's (+0.328) despite arising from a much shallower prior press (6 mm vs. 10 mm) — a strain-path illustration of the central Section 4.4.1 finding that geometric corner overlap can elevate strain severity to a level comparable with a considerably deeper, non-overlapping prior operation, reinforcing that overlap avoidance and prior-depth management are two independent levers on reshaping outcome rather than two expressions of the same underlying variable.

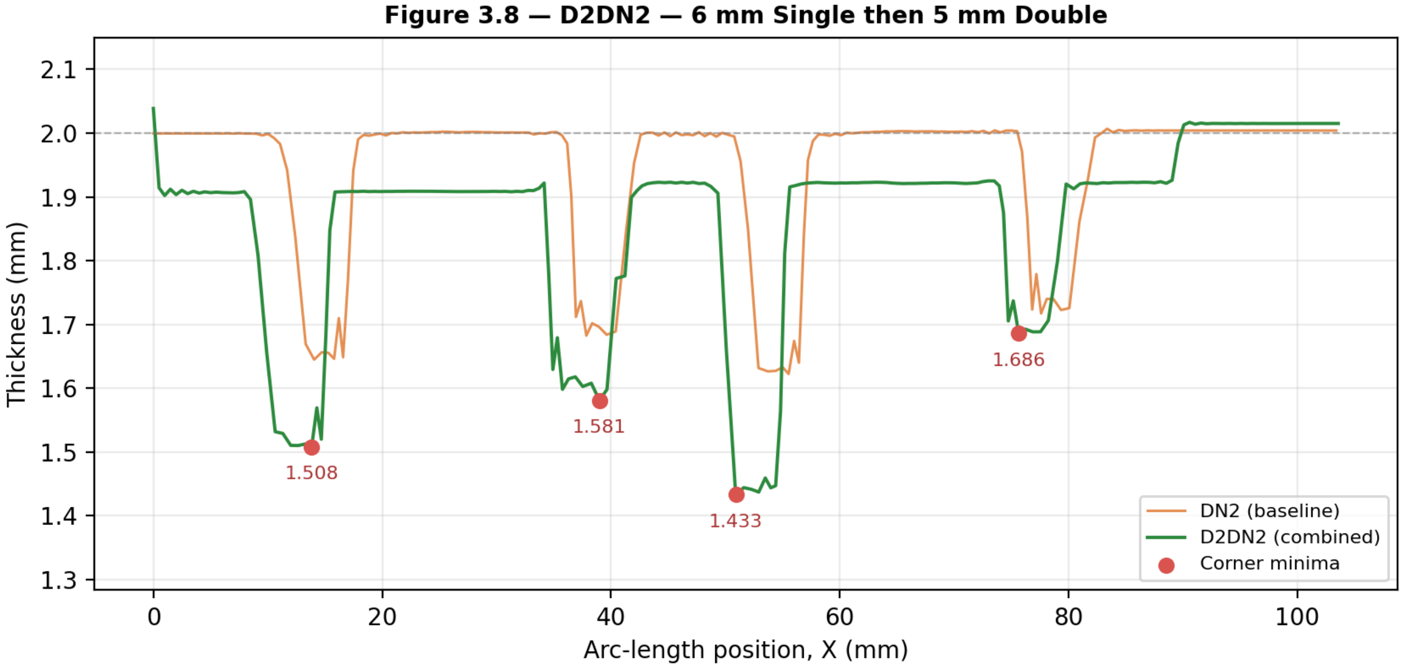

Figure 3.8 — D2DN2 (green) vs. DN2 baseline (orange): geometric overlap drives 28.3% thinning from shallow 6 mm prior press. Corner spread 0.253 mm, roughly 10× the favourable D2DN1 spread.

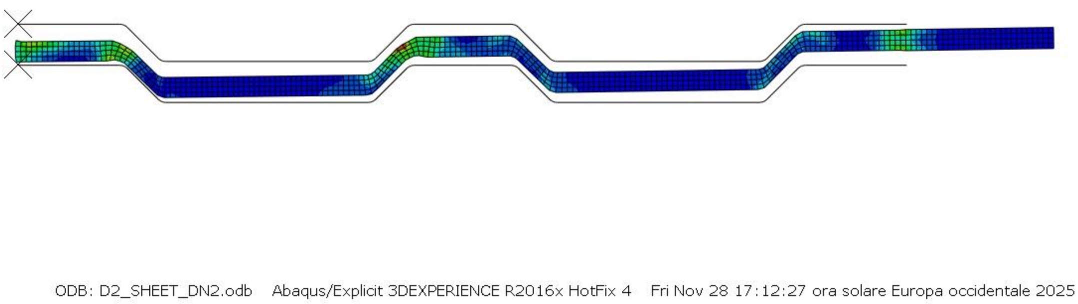

Figure 3.8b — D2DN2 (6 mm single then 5 mm double): deformed blank shape at the final forming increment. Contour shading qualitative.

3.3 Multi-Metric Comparative Analysis

Table 3.1 consolidates all four quantitative metrics for the eight configurations. Figure 3.9 presents grouped thinning bars with the baseline band highlighted. Table 3.2 provides per-corner detail.

Table 3.1 — Summary metrics: minimum thickness, thinning %, maximum gradient, corner spread.

Config	Min t (mm)	Thinning %	Max Gradient (mm/node)	Corner Spread (mm)
D1	1.620	19.0%	0.206	0.017
D2	1.595	20.2%	0.169	0.056
DN1	1.633	18.4%	0.164	0.026
DN2	1.622	18.9%	0.217	0.095
D1DN1	1.328	33.6%	0.375	0.589
D1DN2	1.442	27.9%	0.263	0.487
D2DN1	1.611	19.5%	0.216	0.022
D2DN2	1.433	28.3%	0.247	0.253

Table 3.2 — Per-corner minimum thickness values (mm) for all configurations. D1 and D2 (single-notch tooling) have two corners; all other configurations have four.

Config	Corner 1	Corner 2	Corner 3	Corner 4	Spread (mm)
D1	1.642	1.626	—	—	0.017
D2	1.595	1.651	—	—	0.056
DN1	1.638	1.639	1.632	1.658	0.026
DN2	1.645	1.682	1.622	1.717	0.095
D1DN1	1.409	1.542	1.328	1.917	0.589
D1DN2	1.442	1.453	1.560	1.930	0.487
D2DN1	1.611	1.615	1.618	1.633	0.022
D2DN2	1.508	1.581	1.433	1.686	0.253

Table 3.3 — Additional thinning vs. virgin baseline for combined configurations.

Combined Config	Baseline Ref	Baseline Thinning	Combined Thinning	Additional (pp)	Mechanism
D1DN1	DN1	18.4%	33.6%	+15.2	Deep prior PEEQ + overlap
D1DN2	DN2	18.9%	27.9%	+9.0	Deep prior PEEQ
D2DN1	DN1	18.4%	19.5%	+1.1	Near-zero — shallow prior benign
D2DN2	DN2	18.9%	28.3%	+9.4	Geometric corner overlap

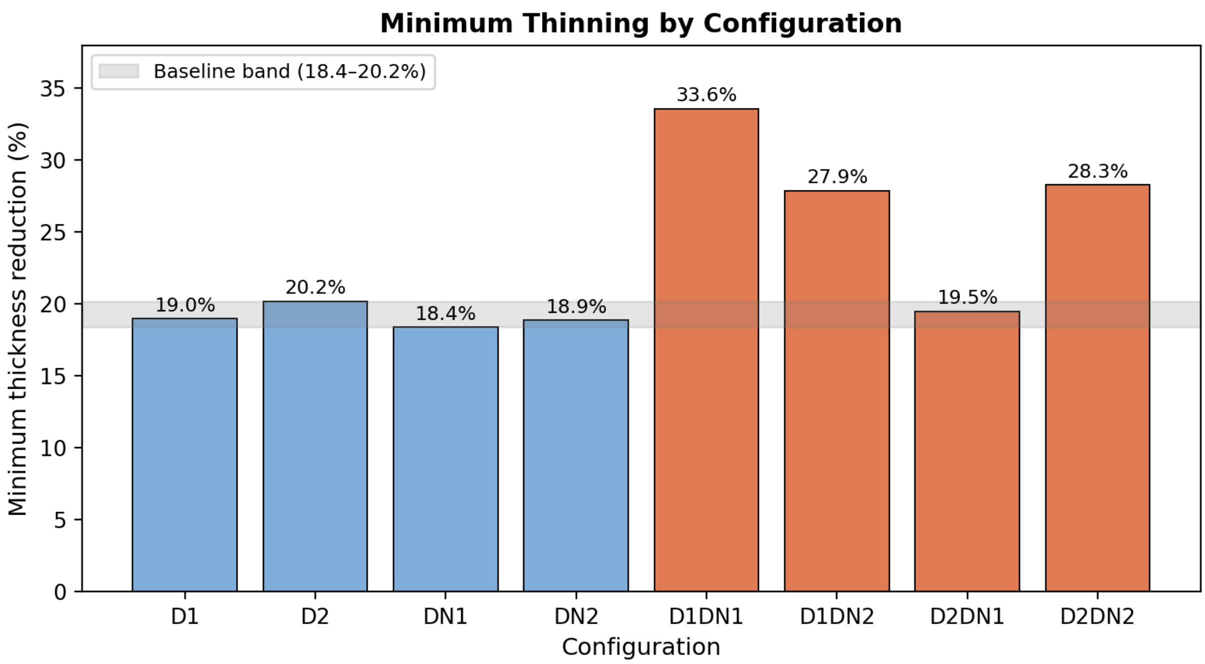

Figure 3.9 — Minimum thinning by configuration. Baseline band (D1, D2, DN1, DN2) shown in blue; combined EoL configurations in orange. Grey band marks the 18.4–20.2% baseline range.

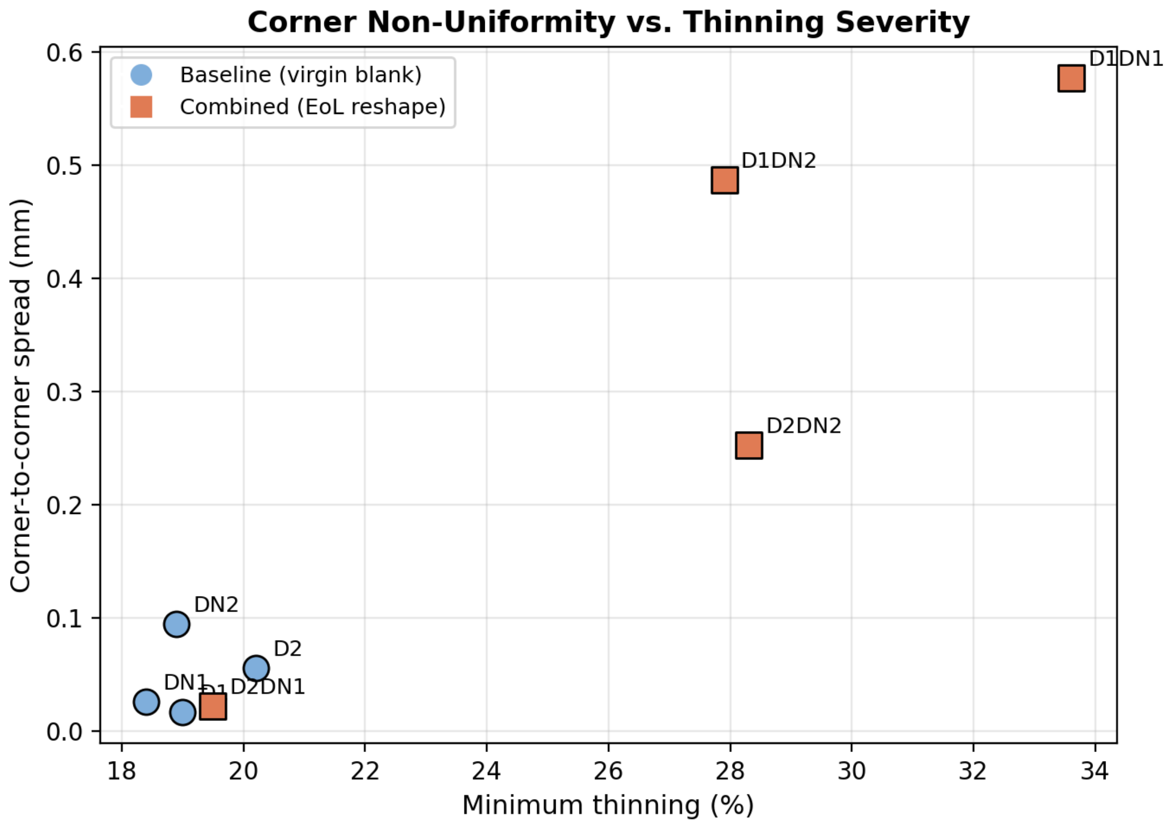

Figure 3.10 — Corner-to-corner spread (mm) vs. minimum thinning (%). Combined configurations (orange squares) show markedly higher non-uniformity than baseline (blue circles) at comparable or lower thinning.

3.3.1 Effect of Prior Forming Depth

Comparing configurations with the same second press but different first-press depth: D1DN1 (deep prior) vs. D2DN1 (shallow prior) for the DN1 second press gives 33.6% vs. 19.5% — a 14.1 pp difference attributable entirely to prior forming depth. This is the clearest isolating comparison in the dataset. Deeper prior history (higher PEEQ) consumes more residual ductility, leaving less margin for the second operation and producing more severe thinning.

3.3.2 Thinning Gradient as Damage Localisation Metric

Baseline gradients: 0.164–0.217 mm/node. Combined range: 0.216 (D2DN1) to 0.375 (D1DN1, +73% above the baseline maximum). Higher gradient indicates more abrupt approach to minimum thickness over a narrower spatial zone — increasing fracture initiation risk for the same minimum thickness level. The gradient ranking (D1DN1 > D1DN2 > D2DN2 > D2DN1) closely parallels thinning severity, confirming the same underlying cumulative strain mechanism governs both metrics — though D1DN2 and D2DN2 swap places relative to their thinning-percentage ranking (D2DN2 has marginally higher thinning than D1DN2 but a lower gradient), indicating that gradient and minimum-thickness, while correlated, are not perfectly redundant measures of severity.

3.3.3 Corner Uniformity and QC Implications

Baseline corner spreads: 0.017–0.095 mm. Combined: 0.022 mm (D2DN1, the tightest of any configuration in the study, baseline included) to 0.589 mm (D1DN1, roughly 23 times the DN1 baseline spread of 0.026 mm). This dramatic increase in non-uniformity for D1DN1 reflects spatially heterogeneous prior strain: different corners of the second-press tooling engage material with very different prior PEEQ. This has a critical QC implication: single-point thickness inspection is inadequate for combined EoL configurations. For D1DN1, one corner (1.917 mm, only 4% thinning) would appear essentially unaffected if measured in isolation, while another (1.328 mm, 33.6%) is near-critical — the difference would be missed entirely by single-point inspection, and would in fact give a badly misleading impression of the part's overall condition.

3.3.4 Feasibility Assessment and Provisional Safe Reshaping Envelope

No fracture was predicted in any configuration. The minimum thickness of 1.328 mm (D1DN1) remains above the approximate fracture threshold for AA6xxx alloys in T6 temper. All eight configurations are feasible within the investigated parameter range. Safety margins are: substantial for D2DN1 (1.1 pp above baseline); moderate for D1DN2 (9.0 pp); reduced for D2DN2 (9.4 pp) and D1DN1 (15.2 pp). The provisional safe reshaping envelope is defined as:

- SAFE: Prior depth ≤6 mm, no geometric corner overlap — thinning ≤19.5% (D2DN1 class). No special process adaptation required.

- CONDITIONAL: Prior depth ≤10 mm with second press ≤5 mm, or any depth with no corner overlap — thinning 19–28%. Explicit multi-point thickness QC required.
- MARGINAL: Prior depth ≥10 mm with second press ≥8 mm (D1DN1 class), or any shallow prior with severe geometric corner overlap (D2DN2 class) — thinning 28–34%. Approach with caution; minimise overlap; full corner inspection mandatory.

3.3.5 Consolidated Strain-Path Estimate Across All Configurations

Sections 3.1 and 3.2 derived, for each configuration in turn, a first-order estimate of the major in-plane strain at the critical corner, using the plane strain relationship $\varepsilon_1 \approx \ln(t_0/t\_min)$ introduced in Section 1.4.1 and applied throughout this chapter. Table 3.4 consolidates these individual estimates alongside each configuration's position relative to the T6 plane strain FLC range (0.10–0.18) quoted in Section 1.4.2, expressed as a margin: the number of strain units separating the configuration's estimated ε_1 from the upper edge of the FLC range (a positive margin means the estimate falls above the cited FLC range; the estimate should then be read as indicative of elevated necking risk under the empirical FLC criterion, not as a direct fracture prediction, per the important caveats on strain-path additivity and FLC validity noted in Sections 1.4.2 and 3.2.1).

Table 3.4 — Consolidated major-strain estimates and FLC margin for all eight configurations.

Config	Min t (mm)	ε_1 estimate	FLC upper bound (T6)	Margin above FLC	Class
D1	1.620	+0.210	0.18	+0.030	Baseline
D2	1.595	+0.226	0.18	+0.046	Baseline
DN1	1.633	+0.202	0.18	+0.022	Baseline
DN2	1.622	+0.209	0.18	+0.029	Baseline
D1DN1	1.328	+0.410	0.18	+0.230	Marginal
D1DN2	1.442	+0.328	0.18	+0.148	Conditional
D2DN1	1.611	+0.216	0.18	+0.036	Safe
D2DN2	1.433	+0.334	0.18	+0.154	Conditional

Two observations follow from Table 3.4 that are not immediately obvious from the thinning-percentage data of Table 3.1 alone. First, every baseline configuration already sits modestly above the cited T6 FLC upper bound (margins of +0.022 to +0.046), a consequence of the conservative choice to compare against the more restrictive T6 (service-condition) FLC rather than the more permissive T4 (as-formed) FLC discussed in Section 1.4.2; had the T4 bound (0.25) been used instead, all four baseline configurations would fall comfortably within the safe region, and only the combined configurations would show any FLC-margin excess at all. This sensitivity to which FLC curve is assumed underscores that the FLC comparison in this thesis is illustrative of relative severity ranking rather than a certified pass/fail fracture criterion, consistent with the qualifications already raised in Section 1.4.2 and Section 3.2.1.

Second, and more informative for the ranking of configurations, the margin gap between D2DN1 (+0.036) and the two "conditional" configurations D1DN2 and D2DN2 (+0.148 and +0.154 respectively) is far larger than the gap between D2DN1 and the baseline group (+0.022 to +0.046) — visually and numerically reinforcing the "safe / conditional / marginal" three-tier classification proposed in Section 3.3.4 on independent, strain-path grounds rather than on the thinning-percentage grounds used to originally define it. The two classification schemes agree closely, which is a useful internal consistency check on the overall feasibility assessment of this thesis, obtained by two different routes from the same underlying nearest-neighbour thickness data.

Chapter 4 — Discussion

4.1 Interpretation of Baseline Results: r/t Dominance

The four baseline configurations establish a 18.4–20.2% thinning band across notch depths of 5–10 mm and both single and double notch geometries — a 1.8 pp width that is remarkably narrow given the 2× range in depth and qualitative geometry change. This indicates that for single-step forming from uniform virgin blanks, the primary parameter governing corner thinning is the punch radius-to-thickness ratio (r/t), not notch depth. All configurations share the same punch corner radius; varying depth within 5–10 mm does not substantially alter the local bending mechanics at the corner, which are governed by r/t.

The counterintuitive elevation of D2 (20.2%) above D1 (19.0%) despite its shallower depth is consistent with this interpretation: the shallower notch creates a more acute corner included angle, slightly reducing the effective corner radius and concentrating bending strain over a shorter arc, increasing peak thinning. This has a practical implication: reducing notch depth to limit deformation is not always the safer choice if it simultaneously reduces the effective corner radius or included angle. Tool design should consider the local r/t ratio, not just depth.

4.2 Prior Deformation History: Mechanistic Interpretation of D2DN1

The D2DN1 finding (19.5% vs. 18.4% baseline, +1.1 pp) is the most practically significant result. Mechanistically: the D2 first press (6 mm) deposits PEEQ of approximately 10–12% at corners, raising flow stress from A = 167 MPa to approximately 260–270 MPa at those locations. When the DN1 second press engages the blank, these pre-hardened corners resist deformation more strongly than the surrounding virgin material, partially redistributing plastic flow to less-strained regions. For the D2 shallow prior press, this redistribution is sufficient to absorb most second-press strain in previously undeformed material, producing a near-virgin outcome overall.

The pre-strained corners have hardened enough to redirect flow, but have not consumed sufficient ductility to constitute a fracture-risk zone. This is a threshold-type behaviour: below a critical prior strain, the work-hardening redistribution effect dominates; above it (D1 conditions), ductility exhaustion dominates. The threshold lies between approximately 12% and 18% PEEQ in the present alloy, corresponding to first-press depths between 6 mm and 10 mm. Identifying this threshold precisely — through intermediate first-press depths at 7, 8 mm — is a priority future work item.

The industrial implication is direct: EoL components originally formed to shallow depths (hood inner panels, door structural inners, brackets with modest contour) can be directly reshaping-routed without special process accommodation. Reshaping outcomes are statistically equivalent to virgin blank forming, eliminating the need for sorting overhead that would be required if all prior deformation were equally damaging.

4.3 Cumulative Damage in D1DN1: Ductility Exhaustion and Non-Uniformity

D1DN1 (33.6% thinning, corner spread ≈22× baseline) represents the extreme end of the parameter space. The D1 prior press (10 mm, PEEQ ≈ 18–20% at corners) consumes roughly 50–55% of the total plastic strain capacity at those locations, assuming a failure strain of 35–45% in T6 condition. The remaining ductility margin (approximately 15–25 pp) is insufficient to absorb the full second-press strain increment without localised thinning progression.

The roughly twenty-three-fold corner non-uniformity (0.589 mm vs. 0.026 mm) reflects spatially heterogeneous prior strain across the blank. The four second-press corners engage material at four different prior strain levels: the most-affected corner (maximum prior PEEQ) produces 1.328 mm; the least-affected corner produces 1.917 mm — only 4% thinning, close to the virgin baseline, indicating that this particular corner of the second press landed on blank material that the first press had left almost entirely undisturbed. This spatial heterogeneity is an intrinsic signature of multi-step forming history. Unlike single-step non-uniformity — which arises from tooling geometry and is predictable from the design — multi-step non-uniformity arises from the interaction between two independent prior operations and requires knowledge of both to predict.

4.4 Geometric Overlap as an Independent Damage Amplifier: The D2DN2 Anomaly

D2DN2 (28.3% thinning from 6 mm + 5 mm operations) demonstrates that geometric overlap between successive press corner positions can amplify thinning to levels exceeding those of much deeper non-overlapping operations. This finding has no clear precedent in the published conventional press forming literature.

The mechanism is straightforward but its practical importance is underappreciated: when the second-press corner position coincides with the first-press corner position, the second operation re-engages the most heavily pre-strained material in the blank, stacking PEEQ increments at the same spatial location. The overlap in D2DN2 is an incidental consequence of the specific notch widths and spacings of the D2 and DN2 tooling geometries, not a deliberate design choice.

4.4.1 Quantifying the Overlap Effect Relative to the Pure Depth Effect

It is useful to decompose the total D2DN2 thinning elevation (9.4 pp above the DN2 baseline, per Table 3.3) into a depth-effect component and an overlap-effect component, using D2DN1 as the reference for the depth effect alone. D2DN1, which shares the identical D2 prior press but uses the non-overlapping DN1 second-press geometry, shows only a 1.1 pp elevation above its own baseline (Section 3.2.3) — establishing that the pure depth effect of a 6 mm prior press, absent overlap, is approximately 1 pp. The remaining 8.3 pp of D2DN2's 9.4 pp elevation (the difference obtained by comparing D2DN2's 9.4 pp total elevation against the 1.1 pp baseline depth effect established by D2DN1) is therefore attributable to the overlap mechanism specifically, not to the inherent severity of the D2 or DN2 geometries considered individually.

This decomposition is only approximate, since D2DN1 and D2DN2 use different second-press geometries (DN1 at 8 mm vs. DN2 at 5 mm) and the comparison is not a perfectly controlled isolation of the overlap variable alone — the shallower DN2 second press might independently be expected to produce somewhat different baseline thinning than DN1 even absent any overlap, as the DN1/DN2 baseline comparison in Section 3.1.4 already shows (18.4% vs. 18.9%, a modest 0.5 pp difference). Given that the DN1/DN2 baseline difference is itself small, the approximation that the residual ~8.3 pp gap between D2DN1 and D2DN2 outcomes is attributable predominantly to overlap rather than to second-press geometry differences is reasonably well supported by the baseline data, but a dedicated controlled experiment — varying corner offset distance at fixed first- and second-press depths — would be needed to fully isolate and quantify the overlap effect as a continuous function of offset distance, as proposed in Section 5.4 (Priority 4).

The practical implication is highly actionable: a simple offset of the second-press tooling position along the blank length to displace its corners away from the first-press corners — achievable through blank repositioning or die offset — would eliminate the overlap mechanism and is expected to restore D2DN2 thinning to D2DN1 levels (approximately 19–20%). This is a zero-cost process improvement requiring no new tooling or material change, only positional adjustment. In digitally-enabled manufacturing environments, the prior-press corner positions are available from the original stamping programme and could be used to automatically compute the optimal second-press offset.

4.5 Comparison with Published EoL Reshaping Literature

Pellegrini et al. (2020) found in SPIF-based EoL reshaping that thinning severity correlated directly with prior equivalent plastic strain, with multiply-formed regions exhibiting 2–3 times the baseline thinning. The present study finds a consistent trend: D1 prior history (~18–20% PEEQ) produces a 1.7–1.8× relative thinning increase compared to D2 prior history (~10–12% PEEQ) for the same second press (comparing D1DN1 vs. D2DN1). This quantitative consistency across fundamentally different forming processes — SPIF vs. conventional press — suggests the prior PEEQ mechanism is robust and process-independent.

Piccininni et al. (2024) found in hydroforming that moderate prior deformation required significant process parameter adjustment relative to virgin blank processing. The present study's D2DN1 finding — that shallow prior deformation requires no process adaptation in conventional press forming — suggests conventional pressing is less sensitive to prior history than hydroforming, likely because rigid tooling imposes the geometry regardless of blank stiffness variation, whereas hydroforming pressure response is sensitive to blank compliance changes induced by prior forming.

Table 4.1 — Present study vs. published EoL reshaping results.

Study	Process	Alloy	Prior Condition	Additional Thinning	Key Finding
Present (shallow)	Conv. press	AA6xxx	D2: 6 mm	+1.1 pp	Near-zero: shallow prior benign
Present (deep)	Conv. press	AA6xxx	D1: 10 mm	+15.2 pp	Significant; geometry management needed
Pellegrini (2020)	SPIF	AA2024-O	Deep drawn	2–3× baseline	PEEQ dominates reshaping outcome
Piccininni (2024)	Hydroforming	AA5754-O	Moderate draw	Process change required	Geometry sensitivity high in hydroforming

4.6 Springback and Dimensional Accuracy Considerations

Springback in AA6xxx T6 ($\sigma_y/E \approx 0.0036$) is approximately 2.4× that of mild steel. For notch depths of 5–10 mm and the present r/t ratios, springback angles of 3–8° are expected at corners based on published data for comparable alloys. In multi-step forming, the residual stress field from the first operation — particularly the tensile residual stress at heavily thinned corners — reduces elastic springback locally (tensile pre-stress reduces the bending moment reversal available upon unloading), while compressive residual stress in adjacent regions increases springback there. The result is a spatially non-uniform springback response producing distorted geometry not predicted by single-step springback analysis.

A first-order estimate of the springback ratio can be obtained from the classical sheet-bending springback formula, $K_s = R_f/R_i = 4(R_i/t \cdot \sigma_y/E)^3 - 3(R_i/t \cdot \sigma_y/E) + 1$, where R_i and R_f are the inner bend radius before and after unloading and t is sheet thickness. Taking a representative inner radius $R_i \approx 4$ mm (consistent with the punch corner radius assumed in Section 1.4.1) and $t = 2$ mm gives $R_i/t = 2$, and with $\sigma_y/E \approx 0.0036$ for the present AA6xxx T6 material, the bracketed term $R_i/t \cdot \sigma_y/E \approx 0.0072$ is small enough that the cubic term is negligible and $K_s \approx 1 - 3(0.0072) \approx 0.978$, implying a springback-driven radius increase of roughly 2%, corresponding to an angular springback of approximately 2–3° for the present geometry — at the lower end of the 3–8° range cited from the literature above, and consistent with the relatively shallow bend angles (depths of 5–10 mm over a 100 mm blank) investigated in this study compared to more severe drawing operations.

This estimate is necessarily approximate: it assumes pure bending without superimposed membrane stretching, whereas the strain-path analysis of Section 3.2.1 establishes that the present forming operations involve substantial membrane stretching alongside bending (the plane strain condition $\varepsilon_1 = -\varepsilon_3$ derived in Section 1.4.1 mixes both contributions). Superimposed tensile membrane strain is known from the springback literature to reduce the springback ratio further by pre-straining the material into a more strain-hardened, lower-elastic-recovery state — meaning the 2–3° estimate above is itself likely an upper bound on the true springback angle for the present forming conditions, though confirming this quantitatively would require the dedicated Abaqus/Implicit relaxation analysis proposed in Section 5.4 (Priority 3) rather than the simplified beam-bending estimate offered here.

This non-uniform springback constitutes an additional challenge for dimensional accuracy in EoL reshaping beyond the thickness non-uniformity quantified in this study. Future work should include an Abaqus/Implicit relaxation step following forming to predict springback angles for each configuration and inform die compensation design. Springback compensation in multi-step EoL forming is a novel problem for which no published design rules currently exist.

4.7 Quantitative Uncertainty Budget

Sections 1.6, 1.9, 2.4, and the discussion above have each identified individual sources of uncertainty affecting the simulation results — the 2D/3D conservatism, the missing Bauschinger effect, the unverified friction coefficient, and the absence of mesh and energy balance verification due to file loss. This section consolidates these into a single quantitative uncertainty budget, distinguishing sources that affect absolute thinning values from those that affect only the comparative (combined-vs-baseline) conclusions, which are the primary deliverable of this thesis.

Geometric conservatism (2D plane strain vs. 3D): estimated +5 to +15 percentage points of thinning relative to a finite-width blank, based on published 2D/3D comparisons for similar bend geometries (Section 1.6.1). This source applies multiplicatively to all eight configurations and therefore affects absolute values substantially while leaving the relative ranking between configurations largely intact, since the lateral-flow relief mechanism does not depend strongly on prior deformation state.

Constitutive model fidelity (missing Bauschinger effect): estimated +5 to +10% underestimation of PEEQ in stress-reversal regions (Section 1.5.2). This source is concentrated in the combined configurations, where stress reversal between the first and second press operations is most likely, and is expected to be largest for D1DN1 and D2DN2 — meaning the true severity gap between combined and baseline configurations may be modestly understated by the present isotropic-hardening simulations, not overstated.

Process parameter uncertainty (friction coefficient, punch geometry): estimated ±3 to ±5 percentage points of absolute thinning per ±50% variation in friction coefficient (Section 4.8). Because the same friction coefficient and punch geometry are applied identically across all eight configurations, this source is substantially self-cancelling in the comparative metrics (Table 3.3, the additional-thinning-versus-baseline figures) even though it materially affects the absolute thinning percentages reported for any single configuration.

Verification gaps (mesh convergence, energy balance — Sections 2.4.3, 2.4.4): unquantified. Unlike the three sources above, for which a directional estimate can be given from the literature, the absence of mesh convergence and energy balance checks for the present model means no quantitative bound can be placed on potential numerical artefacts (mesh-dependent thinning, inertia-driven deformation), beyond noting that the single mesh density used (0.25 mm seed, four elements through thickness) is consistent with seed sizes reported as converged in comparable published bending simulations, and that the explicit time integration scheme is the field-standard choice for this class of contact-dominated forming problem.

Combining these sources, the overall conclusion is that the comparative findings of this thesis — the near-zero D2DN1 effect, the 14.1 pp D1 vs. D2 depth effect, and the geometric overlap mechanism in D2DN2 — are more robust than the absolute thinning percentages reported for any individual configuration, because the dominant uncertainty sources (geometric conservatism, friction) act similarly across baseline and combined configurations and substantially cancel in the difference metrics that form the basis of Chapters 4 and 5. The absolute percentages should be read as order-of-magnitude indicators pending the experimental validation and 3D extension recommended in Section 5.4, not as certified process design values.

4.8 Limitations and Model Uncertainties

The element type code recovered in surviving model notes (CPS4R) is, under standard Abaqus naming convention, a plane stress designation, while this thesis's analysis is described throughout as plane strain (Section 2.4.1). This internal inconsistency in the recovered record could not be resolved given the loss of the original input file, and is the single most consequential open item among this thesis's limitations, since plane stress and plane strain formulations are not mechanically equivalent for a bending-and-stretching problem of the kind studied here: plane stress permits free out-of-plane (width-direction) strain where plane strain suppresses it entirely, and the choice directly affects predicted thinning severity. All comparative conclusions in this thesis (Section 3.3, Chapter 4) rely on differences between configurations computed under whichever single formulation was actually used, and remain internally valid regardless of which it was; however, the absolute thinning percentages, and any comparison of this thesis's absolute values against the published literature using a confirmed plane strain formulation (Section 4.5), should be treated with this caveat in mind pending model reconstruction (Section 5.4, Priority 0).

The 2D idealisation (whether ultimately confirmed as plane stress or plane strain) is in either case expected to differ from real 3D forming, where lateral material flow in a finite-width blank provides an additional strain relief mechanism not available in a 2D cross-sectional model. Published 2D vs. 3D comparisons for plane strain forming geometries suggest a 5–15% reduction in corner thinning under 3D conditions; the equivalent 2D-to-3D offset for a plane stress formulation has not been separately established in this thesis and would need to be assessed once Priority 0 confirms the element formulation actually used. The Johnson-Cook isotropic hardening model does not capture the Bauschinger effect; regions with stress reversal between operations may accumulate 5–10% higher PEEQ than predicted. This is insufficient to change qualitative conclusions but is a source of quantitative uncertainty.

The friction coefficient ($\mu = 0.1$) and punch corner geometry were specified from typical literature values without experimental verification for this specific alloy-tooling combination. A ±50% variation in friction ($\mu = 0.05$ to 0.15) would produce approximately ±3–5 pp variation in absolute corner thinning. Comparative results (combined vs. baseline, with identical friction applied to both) are substantially more robust to this uncertainty than absolute thinning values. No physical experimental validation has been performed; results are simulation predictions based on literature-calibrated material parameters. As discussed in Sections 2.4.3 and 2.4.4, formal mesh convergence and energy balance verification — the standard validation steps for a mass-scaled Abaqus/Explicit study — could not be performed for this thesis following the loss of the original model files, and are flagged here as the most significant open numerical verification gap relative to standard practice in the field, alongside the element formulation question above.

4.9 Industrial Implications and Process Design Guidance

The results provide the first quantitative numerical basis for process design guidelines for conventional press-based EoL reshaping of AA6xxx aluminium sheet.

Prior deformation depth sorting is the most leveraged single intervention. The 14.1 pp difference between D1DN1 and D2DN1 for the same reshaping operation establishes that reshaping outcomes depend strongly on prior history. EoL components should be classified into shallow-history (≤6 mm equivalent depth: safe, no adaptation) and deep-history (≥8 mm: requires reduced second-press geometry or explicit thickness verification) categories before entering a reshaping production line.

Corner position planning to avoid geometric overlap is a zero-cost intervention that eliminates the D2DN2-class anomaly. For components routed to reshaping, mapping prior-press corner positions onto the blank and selecting a second-press offset that maximises corner separation eliminates the amplification mechanism demonstrated in D2DN2. In digital manufacturing environments, this computation is straightforward from existing stamping programme data.

Multi-point thickness QC is essential. The factor-of-twelve corner non-uniformity in D1DN1 makes single-point inspection statistically unreliable. A mandatory per-corner measurement protocol (minimum one measurement per bend corner) is required. For high-value components, automated ultrasonic thickness scanning across the full bend length provides comprehensive coverage.

Table 4.2 — Provisional safe reshaping process window for AA6xxx sheet (t_0 = 2 mm, plane strain, no corner overlap).

Scenario	Prior Depth	Second Depth	Predicted Thinning	Safety Margin	Recommendation
D2DN1 class	≤6 mm	5–8 mm (no overlap)	≤19.5%	Large	Direct reshaping, standard QC
D1DN2 class	≤10 mm	≤5 mm	27.9%	Moderate	Reshaping with multi-point thickness QC
D2DN2 class	≤6 mm	5 mm (with overlap)	28.3%	Reduced	Eliminate overlap; re-assess
D1DN1 class	≥10 mm	≥8 mm	33.6%	Minimum	Use with caution; full QC mandatory

4.9.1 Economic Framing of the Recommended Interventions

The three interventions proposed above differ markedly in cost and implementation complexity, which is relevant to how an industrial adopter would realistically sequence them. Corner position planning (the second intervention) requires no capital investment: it is a die-positioning or blank-orientation decision that can be implemented in software once prior-press corner location data is available, and the present study's D2DN1/D2DN2 comparison (Section 4.4.1) suggests it alone can recover the majority of the thinning penalty associated with geometric overlap. This makes it the natural first intervention for any organisation beginning to explore EoL reshaping, since it requires no new equipment and can be validated quickly against a small batch of components.

Prior deformation depth sorting (the first intervention) requires either retained forming-history data (the digital product passport scenario discussed in Section 1.9) or a physical measurement step at the EoL recovery facility — portable thickness gauging, for instance, is a mature, relatively low-cost technology already used in automotive body shops for collision repair assessment, and could plausibly be repurposed for this sorting task without major new capital investment. The marginal cost is primarily in process time (an additional measurement and classification step per incoming EoL component) rather than equipment, and scales with reshaping line throughput rather than being a fixed cost.

Multi-point thickness QC (the third intervention) has the widest range of plausible implementation cost, from a low-cost option (manual point-gauge measurement at four corner locations, requiring only operator time) to a higher-cost option (automated ultrasonic thickness scanning across the full bend length, requiring dedicated scanning equipment and line integration). For an initial pilot deployment of conventional press EoL reshaping, the manual measurement approach would likely be the appropriate starting point given its low capital cost, with automated scanning considered as a scale-up investment once reshaping volumes justify the equipment cost — broadly analogous to the way many quality inspection processes in automotive manufacturing have historically progressed from manual sampling to automated 100% inspection as production volumes and quality requirements increased.

This economic framing is necessarily qualitative, since this thesis has not conducted a dedicated cost-benefit analysis (that exercise is explicitly proposed as part of the industrial case study, Section 5.4 Priority 6); it is included here to make clear that the recommendations of this chapter are intended to be incrementally adoptable rather than requiring a single large up-front investment, which is a relevant practical consideration for any organisation deciding whether to begin piloting EoL reshaping on the basis of this thesis's findings.

Chapter 5 — Conclusions and Future Work

5.1 Summary of Principal Findings

This thesis presents the first systematic numerical characterisation of thickness distribution in aluminium alloy sheet subjected to single-step and two-step conventional press forming operations representing end-of-life reshaping scenarios. Eight configurations were investigated using 2D plane strain FEA in Abaqus/Explicit with Johnson-Cook constitutive modelling. The six principal findings are:

Finding 1 — Tight baseline thinning band: Single-step forming from virgin blanks produces 18.4–20.2% corner thinning across all notch depths (5–10 mm) and geometries (single and double notch) investigated. The dominant parameter is the punch corner radius-to-thickness ratio, not notch depth. This robust, low-scatter baseline enables clear quantification of prior-history effects in combined configurations.

Finding 2 — Shallow prior history is benign: Blanks pre-formed to 6 mm depth (D2, PEEQ ≈ 10–12% at corners) produce only 1.1 percentage points more thinning than virgin blanks in the subsequent 8 mm double-notch reshaping (D2DN1: 19.5% vs. DN1 baseline 18.4%). Shallow prior deformation does not meaningfully compromise formability in conventional press reshaping.

Finding 3 — Deep prior history imposes substantial additional thinning: Blanks pre-formed to 10 mm depth (D1, PEEQ ≈ 18–20%) produce 33.6% thinning under the 8 mm second press (D1DN1) — 15.2 pp above baseline — with a roughly twenty-three-fold increase in corner non-uniformity (spread 0.589 mm vs. 0.026 mm baseline).

Finding 4 — Geometric overlap is an independent damage amplifier: D2DN2 (6 mm + 5 mm with overlap) produces 28.3% thinning despite shallower operations than D1DN1, because second-press corners re-engage first-press corner locations. Corner position planning is a first-order process variable in multi-step EoL reshaping.

Finding 5 — The overlap effect dominates the depth effect at shallow prior history: decomposing the D2DN2 result (Section 4.4.1) shows that approximately 8.3 of its 9.4 percentage point elevation above baseline is attributable to geometric corner overlap rather than to the inherent severity of the 6 mm prior press, which in isolation (D2DN1) produces only a 1.1 pp elevation. For shallow-history components, tooling position is therefore a larger lever on reshaping outcome than prior forming depth itself.

Finding 6 — All configurations remain below the fracture threshold: No fracture was predicted in any of the eight configurations. The 2D plane strain results are conservative upper bounds; 3D forming would produce 5–15% less thinning. Conventional press reshaping is feasible across the full investigated parameter range, with safety margin decreasing for D1DN1 and D2DN2.

Taken together, these six findings support a central thesis-level conclusion: the feasibility of conventional press-based EoL reshaping for AA6xxx aluminium sheet is governed less by the absolute magnitude of prior or subsequent forming depth than by two more specific and more controllable variables — the prior strain accumulated at the specific corners that will be re-engaged by the second press, and the spatial alignment between first-press and second-press corner positions. Both variables are, in principle, knowable and manageable at the process design stage (Section 4.9), which is the basis for this thesis's overall assessment that conventional press EoL reshaping is a technically viable circular economy strategy for this alloy class, subject to the experimental validation and 3D extension recommended in Section 5.4.

5.2 Practical Recommendations

Recommendation 1 — Prior depth sorting: Classify EoL aluminium sheet components into shallow-history (≤6 mm equivalent depth: safe, standard process) and deep-history (≥8 mm: reduced second-press depth or explicit QC required) categories before reshaping-line routing.

Recommendation 2 — Corner position planning: Map first-press corner positions onto the EoL blank and offset second-press tooling to maximise corner separation. This eliminates the D2DN2-class geometric overlap anomaly at zero additional cost, and per Finding 5 above is likely the single highest-leverage intervention available for shallow-history components specifically.

Recommendation 3 — Multi-point thickness QC: Mandate per-corner thickness measurement (minimum one point per bend corner) for all combined EoL configurations. Single-point inspection is statistically unreliable given the up to ≈22-fold corner non-uniformity observed.

Recommendation 4 — Use the provisional reshaping envelope as an initial screening tool: Apply the Table 4.2 process window for first-pass component feasibility assessment, pending experimental validation.

Recommendation 5 — Sequence interventions by cost: Implement corner position planning first (zero capital cost), prior depth sorting second (low cost, primarily process time), and automated multi-point QC last (variable cost, scalable with reshaping volume), consistent with the economic framing discussed in Section 4.9.1. This sequencing allows an organisation to begin realising the environmental and economic benefits of reshaping (Section 1.2) without requiring a single large up-front capital commitment.

5.3 Research Limitations

The study is subject to the following limitations. 2D plane strain overestimates thinning by 5–15% relative to real 3D finite-width forming; results are conservative upper bounds. Johnson-Cook isotropic hardening omits the Bauschinger effect; 5–10% PEEQ underestimation in stress-reversal regions is possible. Friction and geometry parameters are literature-based without specific experimental verification, introducing ±3–5 pp quantitative uncertainty in absolute thinning. No physical experimental validation has been performed. The parameter space covers notch depths 5–10 mm and two notch geometries only; extrapolation to deeper operations, different blank thicknesses, or other alloys requires additional data.

5.4 Roadmap for Future Work

Seven research priorities are identified, ordered by scientific urgency and expected industrial impact. Priority 0 is listed separately from the original six-item roadmap because it is a prerequisite recovery step specific to this thesis's circumstances rather than a new scientific direction; Priorities 1 through 6 represent the substantive research programme.

Priority 0 — Model reconstruction and verification (immediate, prerequisite to all else): Rebuild the eight Abaqus/Explicit models from the surviving geometry sketches, material parameters, and boundary condition records documented in this thesis. Confirm the element formulation actually used (resolving the plane stress/plane strain discrepancy flagged in Section 2.4.1 and Section 4.8 — the single highest-priority item within this reconstruction effort, given its direct bearing on absolute thinning magnitude). Re-run mesh convergence (coarse/medium/fine seed comparison), energy balance (KE/IE) monitoring, and friction coefficient sensitivity — verification steps that could not be completed for this submission due to file loss — and confirm that the reconstructed models reproduce the surviving CSV thickness data (Section 2.5.1) within reasonable tolerance. This step should be completed before any of Priorities 1 through 6 are pursued, since it re-establishes a verified simulation baseline; estimated effort is one to two weeks for an analyst already familiar with the model geometry, given that the die and punch sketches, material card, and boundary condition setup are all documented in Chapter 2 and Figures 2.1–2.3.

Priority 1 — Experimental validation (highest scientific urgency): Manufacture physical specimens under the same press conditions. Measure thickness by cross-section optical microscopy or structured-light 3D scanning. Validate JC parameters against D1 and DN1 baselines; confirm D2DN1 near-baseline finding and D2DN2 geometric overlap anomaly. Experimental confirmation is the single step most critical to credibility of the industrial recommendations, and should follow directly from Priority 0 since a verified simulation baseline is needed to design the specimen press schedule. Estimated effort: four to six weeks including specimen procurement, pressing, sectioning, and measurement, assuming access to a press and a metallography or 3D scanning facility — both of which are typically available within a university mechanical engineering department.

Priority 2 — 3D shell element extension: Re-simulate all configurations using S4R reduced-integration shell elements with a representative blank width of 300–500 mm. Quantify the conservative offset of 2D predictions relative to 3D; produce full surface thinning contour maps; include Hill (1948) anisotropic yield criterion. This priority can proceed in parallel with Priority 1, since it requires only the reconstructed model (Priority 0) and does not depend on experimental results, though final calibration of the 3D model's friction and anisotropy parameters would benefit from the experimental data once available.

Priority 3 — Springback analysis: Add Abaqus/Implicit relaxation steps to all forming simulations. Predict springback angles for each configuration; quantify asymmetric springback in D1DN1 and D2DN2; provide angles as input for die compensation design for EoL reshaping tooling. This is a comparatively low-cost addition once Priority 0 is complete, since it reuses the existing forming step output as the initial condition for a subsequent static relaxation step, requiring no new geometry or material characterisation.

Priority 4 — Parameter densification: Conduct a 4×4 DOE (first-press depth 4–10 mm × second-press depth 3–10 mm) plus corner offset distance as a third parameter. Fit a response surface model for rapid process screening; produce a continuous safe-zone map replacing the four discrete combined-configuration points of the present study. This priority is best sequenced after Priority 1, so that the denser parameter grid can be calibrated against at least one experimentally confirmed data point rather than relying purely on simulation.

Priority 5 — Multi-alloy study: Extend to AA5xxx (Al-Mg, H-temper, higher strain hardening exponent) and AA7xxx (T73, overaged) to establish whether the reshaping envelope limits are alloy-specific. AA5xxx is relevant to structural inner panels; its higher n-value is expected to produce a more forgiving envelope. This priority is independent of Priorities 1–4 and could be pursued by a separate researcher in parallel, since it primarily requires substituting alternative Johnson-Cook parameter sets into the existing (or 3D-extended) model framework.

Priority 6 — Industrial case study: Partner with an automotive OEM or Tier-1 supplier to apply the reshaping framework to a real EoL component. Quantify LCA CO_2 reduction per component cycle, economic comparison versus secondary smelting, and quality conformance rate under real process variability. This case study is the terminal step translating academic findings into deployable manufacturing practice and is realistically sequenced last, since it depends on the credibility established by Priorities 0–4 to be a viable basis for industrial partnership discussions.

Table 5.1 — Future work priority matrix.

Priority	Research Question	Methodology	Expected Outcome
0	Model reconstruction	Rebuild from documented geometry/material/BC records	Verified simulation baseline; mesh + energy checks
1	Experimental validation	Physical specimens, cross-section microscopy / 3D scan	JC parameter calibration; confirm key findings
2	3D shell extension	Abaqus S4R, Hill anisotropy, 300–500 mm width	Quantify 2D conservatism; 3D thinning maps
3	Springback prediction	Abaqus/Implicit relaxation step post-forming	Springback angles; die compensation inputs
4	Parameter densification	4×4 DOE + corner offset; RSM fitting	Continuous safe reshaping envelope map
5	Multi-alloy study	AA5xxx, AA7xxx JC parameters	Alloy-independent vs. alloy-specific envelope
6	Industrial case study	OEM collaboration; LCA, economics, conformance rate	Deployable guidelines; CO_2 quantification

References

[1] Cooper, D.R., and Allwood, J.M. (2012). Reusing Steel and Aluminum Components at End of Product Life. Environmental Science & Technology, 46(18), 10334–10340. https://doi.org/10.1021/es301093a.

[2] Pellegrini, D., Volk, W., and Fratini, L. (2020). Re-forming end-of-life components through single point incremental forming. Journal of Manufacturing Processes, 56, 1355–1366. https://doi.org/10.1016/j.jmapro.2020.04.047.

[3] Piccininni, A., Cusanno, A., Palumbo, G., Strano, M., and Gagliardi, F. (2024). Improving quality of reshaped EoL components via sheet hydroforming. Journal of Manufacturing and Materials Processing, 8(6), 253. https://doi.org/10.3390/jmmp8060253.

[4] Ingarao, G., Zaheer, O., and Fratini, L. (2017). Energy and material efficiency of sheet metal forming processes: A review. Journal of Manufacturing Processes, 27, 53–65. https://doi.org/10.1016/j.jmapro.2017.04.004.

[5] Ellen MacArthur Foundation (2013). Towards the Circular Economy: Economic and Business Rationale for an Accelerated Transition. Cowes, UK: Ellen MacArthur Foundation.

[6] European Commission (2020). A New Circular Economy Action Plan: For a Cleaner and More Competitive Europe. COM(2020) 98 final. Brussels.

[7] European Commission (2019). The European Green Deal. COM(2019) 640 final. Brussels.

[8] Keeler, S.P., and Backofen, W.A. (1963). Plastic instability and fracture in sheets stretched over rigid punches. ASM Transactions Quarterly, 56, 25–48.

[9] Goodwin, G.M. (1968). Application of strain analysis to sheet metal forming in the press shop. SAE Technical Paper 680093. https://doi.org/10.4271/680093.

[10] Johnson, G.R., and Cook, W.H. (1983). A constitutive model and data for metals subjected to large strains, high strain rates and high temperatures. Proceedings of the 7th International Symposium on Ballistics, The Hague, 541–547.

[11] Hill, R. (1948). A theory of the yielding and plastic flow of anisotropic metals. Proceedings of the Royal Society of London, Series A, 193(1033), 281–297.

[12] Dassault Systèmes (2016). Abaqus/Explicit User's Manual, Version 3DEXPERIENCE R2016x. Providence, RI: Dassault Systèmes Simulia Corp.

[13] Banabic, D. (2010). Sheet Metal Forming Processes: Constitutive Modelling and Numerical Simulation. Berlin: Springer. https://doi.org/10.1007/978-3-540-88113-1.

[14] Baudouin, C., Bigot, R., and Pham, H.T. (2020). Remanufacturing and reshaping of aluminium automotive parts: An energy and environmental assessment. Resources, Conservation and Recycling, 155, 104669.

[15] Allwood, J.M., and Cullen, J.M. (2012). Sustainable Materials With Both Eyes Open. Cambridge: UIT Cambridge.

[16] Kalpakjian, S., and Schmid, S.R. (2014). Manufacturing Engineering and Technology, 7th ed. New Jersey: Pearson Education.

[17] Dieter, G.E. (1986). Mechanical Metallurgy, 3rd ed. New York: McGraw-Hill.

[18] Hosford, W.F., and Caddell, R.M. (2011). Metal Forming: Mechanics and Metallurgy, 4th ed. Cambridge: Cambridge University Press.

[19] Tekkaya, A.E. (2000). State-of-the-art of simulation of sheet metal forming. Journal of Materials Processing Technology, 103(1), 14–22.

[20] Marciniak, Z., Duncan, J.L., and Hu, S.J. (2002). Mechanics of Sheet Metal Forming. Oxford: Butterworth-Heinemann.

Appendix A — Full Corner Coordinate Data

This appendix tabulates the full arc-length position (X, mm) and nearest-neighbour thickness (t, mm) for every identified corner in all eight configurations, extending the summary already given in Table 3.2. Values are as computed by the extraction method described in Section 2.5.1, applied to the surviving nodal coordinate CSV export. X positions are measured from the left end of the deformed blank arc length and therefore differ slightly between configurations, since the total deformed arc length varies with forming severity (Section 2.5). These tables are provided for completeness and to support independent recalculation of any derived metric in Chapter 3 without requiring re-access to the original CSV file.

A.1 Baseline Configurations

Table A.1 — D1 (10 mm single notch, virgin blank): full corner data.

Corner #	X position (mm)	Thickness (mm)	Thinning (%)
1	14.6	1.642	17.9%
2	40.8	1.626	18.7%

Table A.2 — D2 (6 mm single notch, virgin blank): full corner data.

Corner #	X position (mm)	Thickness (mm)	Thinning (%)
1	12.2	1.595	20.2%
2	38.3	1.651	17.4%

Table A.3 — DN1 (8 mm double notch, virgin blank): full corner data.

Corner #	X position (mm)	Thickness (mm)	Thinning (%)
1	10.7	1.638	18.1%
2	40.3	1.639	18.1%
3	55.6	1.632	18.4%
4	85.2	1.658	17.1%

Table A.4 — DN2 (5 mm double notch, virgin blank): full corner data.

Corner #	X position (mm)	Thickness (mm)	Thinning (%)
1	14.0	1.645	17.8%
2	37.8	1.682	15.9%
3	55.5	1.622	18.9%
4	77.6	1.717	14.2%

A.2 Combined EoL Configurations

Table A.5 — D1DN1 (10 mm single then 8 mm double): full corner data.

Corner #	X position (mm)	Thickness (mm)	Thinning (%)
1	10.4	1.409	29.6%
2	45.4	1.542	22.9%

Corner #	X position (mm)	Thickness (mm)	Thinning (%)
3	56.9	1.328	33.6%
4	85.5	1.917	4.1%

Table A.6 — D1DN2 (10 mm single then 5 mm double): full corner data.

Corner #	X position (mm)	Thickness (mm)	Thinning (%)
1	10.1	1.442	27.9%
2	45.4	1.453	27.4%
3	56.8	1.560	22.0%
4	80.5	1.930	3.5%

Table A.7 — D2DN1 (6 mm single then 8 mm double): full corner data.

Corner #	X position (mm)	Thickness (mm)	Thinning (%)
1	12.7	1.611	19.5%
2	38.9	1.615	19.3%
3	56.0	1.618	19.1%
4	85.7	1.633	18.4%

Table A.8 — D2DN2 (6 mm single then 5 mm double): full corner data.

Corner #	X position (mm)	Thickness (mm)	Thinning (%)
1	13.8	1.508	24.6%
2	39.0	1.581	20.9%
3	50.9	1.433	28.3%
4	75.6	1.686	15.7%

Cross-checking these tables against Table 3.1: each configuration's reported minimum thickness matches the lowest value among its own corner entries above, and each reported corner spread matches the difference between the highest and lowest thickness value in the relevant table. This internal consistency was verified programmatically before the summary tables of Chapter 3 were finalised, and is provided here so that a reader who wishes to recompute a derived metric — for example, an alternative definition of spread, or a different strain-path formula — can do so directly from this appendix without needing access to the original CSV file.